DOI: https://doi.org/10.2138/am-2022-8594. http://www.minsocam.org/

Revision 2

Word Count (6081)

Melting and melt segregation processes controlling granitic melt composition

Yang Yu [a,b], Xiao-Long Huang [a,b*], Roberto F. Weinberg [c], Min Sun [d], Peng-Li He [a,b], Le Zhang [a]

[a] State Key Laboratory of Isotope Geochemistry, CAS Center for Excellence in Deep Earth Science, Guangzhou Institute of Geochemistry, Chinese Academy of Sciences, Guangzhou 510640, China

[b] Southern Marine Science and Engineering Guangdong Laboratory (Guangzhou), Guangzhou 511458, China

[c] School of Earth, Atmosphere and Environment, Monash University, Clayton, VIC 3800, Australia

[d] Department of Earth Sciences, The University of Hong Kong, Pokfulam Road, Hong Kong

[*]Corresponding author. Xiao-Long Huang, Tel.: (+86) 20-85290010

E-mail address: xlhuang@gig.ac.cn (Xiao-Long Huang)

DOI: https://doi.org/10.2138/am-2022-8594. http://www.minsocam.org/

ABSTRACT

Several important processes in the petrogenesis of granite are still debated due to poor understanding of complex interactions between minerals during the melting and melt segregation processes. To promote improved understanding of the mineral-melt relationships, we present a systematic petrographic and geochemical analysis for melanosome and leucosome samples from the Triassic Jindong migmatite, South China. Petrographic observations and zircon U-Pb geochronology indicate that the Jindong migmatite was formed through water-fluxed melting of the Early Paleozoic gneissic granite (437±2 Ma) during the Triassic (238±1 Ma), with the production of melt dominated by the breakdown of K-feldspar, plagioclase and quartz. The Jindong leucosomes may be divided into lenticular and net-structured types. Muscovite, plagioclase and K-feldspar in the net-structured leucosome show higher Rb and much lower Ba and Sr contents than those in the lenticular leucosome. This may be attributed to elevation of Rb and decreasing Ba and Sr abundances in melts during the segregation process, due to early fractional crystallization of K-feldspar and plagioclase. These leucosomes show negative correlation between $\varepsilon_{Nd}(t)$ and P_2O_5, reflecting increasing dissolution of low $\varepsilon_{Nd}(t)$ apatite during melting process. The continuous dissolution of apatite caused saturation of monazite and xenotime in melt, resulting in the growth of monazite and xenotime around apatite in the melanosome. This process resulted in a sharp decrease of Th, Y and REE with increasing P_2O_5 in the leucosome samples. This complex interplay of accessory mineral reactions in the source impact REE geochemistry and Nd isotope ratios of granites. As the granites worldwide exhibit similar compositional and isotopic patterns with the Jindong leucosomes, we suggest that both

the melting and melt segregation processes strongly control the granitic melt compositions.

Key words: Migmatite; Crustal anatexis; Disequilibrium melting; Chemical fractionation; Granite.

INTRODUCTION

Anatexis and the generation of felsic melts are fundamental processes for chemical differentiation of the continental crust (Kemp and Hawkesworth, 2003; Rudnick and Gao, 2003; Korhonen et al., 2010). Compositions of granite vary significantly due to complex reactions between minerals and melts during processes involved in the generation and segregation of granitic melts (Le Breton and Thompson, 1988; Wyllie and Wolf, 1993; Kriegsman, 2001; Kemp and Hawkesworth, 2003; Farina and Steven, 2011; Brown, 2013; Clemens and Stevens, 2016). For example, residual K-feldspar and plagioclase after the dehydration melting of biotite and amphibole (Le Breton and Thompson, 1988; Wyllie and Wolf, 1993) will cause elevation of Rb and decreasing Ba and Sr in the melt due to high compatibility for Ba and Sr in these feldspar minerals (Zhang et al., 2004; Gao et al., 2017). On the other hand, K-feldspar and plagioclase may preferentially break down during water-fluxed melting processes (e.g., Vernon et al., 2003), releasing more Ba and Sr than Rb into melts and resulting in low Rb/Ba and Rb/Sr ratios of granite.

The behaviors of minerals during the melting and melt segregation processes are still poorly understood, which has caused continued debate on petrogenesis of granite (Zeng et al., 2005; Farina et al., 2014; Clemens and Stevens, 2016). For instance, experimental results suggest that garnet will be a major residual phase during high pressure melting of metasedimentary (5–7 kbar) and meta-igneous rocks (>10 kbar; Le Breton and Thompson, 1988; Wyllie and Wolf, 1993), which may result in low heavy rare earth element (HREE) abundances and high La/Yb ratio in granitic magmas due to high compatibility of HREE in garnet (e.g., Moyen, 2009). However, a school of researchers argue that rare earth element (REE) abundance in granites could be dominated by dissolution of phosphate minerals (monazite, xenotime and apatite) during melting in the source (Ayres and Harris, 1997; Zeng et al., 2005; Farina and Steven, 2011; Farina et al., 2014). This may be deduced by the negative correlation between ε_{Nd}(t) and P_2O_5 for granites worldwide (Fig. S1; Zeng et al., 2005). On the other hand, felsic melts would be segregated away from the source (Sawyer, 2001; Brown, 2013; Clemens and Stevens, 2016), after the volume of melts in source crosses a threshold value of "rheologically critical melt percentage" (~ 5–7 %; Rosenberg and Handy, 2005). During the segregation, melts may undergo entrainment of minerals from the residuum (Chappell et al., 1987; Wolfram et al., 2017), or fractional crystallization along melt migration paths (Brown et al., 2016). The interactions between mineral and melts during the segregation may also significantly modify composition of granitic melts (Chappell et al., 1987; Brown et al., 2016; Koblinger and Pattison, 2017), but has been commonly overlooked due to lack of information for the source (Schwindinger et al., 2020).

Migmatites are heterogeneous and consist of leucosome (leucocratic part formed from a melt) and melanosome (melt-depleted part consisting predominantly of solid residuum after segregation of some, or all of the melt), which record the melting process of metasedimentary or meta-igneous rocks (Sawyer, 2008; Koblinger and Pattison, 2017). Many migmatite domes are spatially and temporally associated with granitic plutons in orogenic belts and have been inferred to be a link between high-grade metamorphism and large-scale granitic bodies (e.g., Brown, 2013). Thus, the mineral assemblage, texture and chemical composition of migmatites may provide evidence for complex interactions of minerals during the melting reactions and segregation of granitic melts (Sawyer et al., 2001; Brown, 2013).

The South China Block is one of the biggest silicic large igneous provinces (~22,000 km^2) worldwide with emplacement of voluminous granites during the Early Paleozoic, Triassic and Jurassic-Cretaceous (e.g., Wang et al., 2012; 2013a; Huang et al., 2013; Yu et al., 2016, 2018; Gao et al., 2017). The granites in the South China Block consist of strongly peralumious S-type and metaluminous I-type granites, which were generated through partial melting of sedimentary or igneous rocks, respectively (Huang et al., 2013; Wang et al., 2013a; Gao et al., 2017; Yu et al., 2018). Extensive migmatites, associated with high-grade metamorphism, were developed coevally with emplacement of granites in the South China Block (Chen and Huang, 1994; Wang et al., 2012). These migmatites are mainly exposed in the northern Wuyi domain and southern Yunkai domain of the Cathaysia Block, and commonly show transitional contacts with granitic plutons, suggesting their close petrogenetic relationship (e.g., Wang et al., 2012, 2013a, b). In this study, we present zircon U-Pb geochronology, *in situ* mineral major and trace element, *in situ* apatite Nd isotope and whole-rock geochemistry and Nd isotope on a suite of migmatite samples from the Jindong area in the Yunkai domain (Fig. 1). The intent is to constrain the complex mineral interactions during melting and melt segregation processes and their influences on the geochemical composition of granitic melts.

<Fig. 1>

Geological background and rock types

Geological background

This is the peer-reviewed, final accepted version for American Mineralogist, published by the Mineralogical Society of America.
The published version is subject to change. Cite as Authors (Year) Title. American Mineralogist, in press.
DOI: https://doi.org/10.2138/am-2022-8594. http://www.minsocam.org/

The South China Block consists of the Yangtze Block in the northwest and the Cathaysia Block in the southeast (Fig. 1a; Wang et al., 2013a and references therein). The Yunkai domain, located in the southwestern Cathaysia Block, is separated from the western Darongshan domain by the Luchuan-Cenxi fault zone and bounded by the Wuchuan-Sihui fault zone in the east (Fig. 1b; e.g., Lin et al., 2008). The Yunkai domain consists of Neoproterozoic-Ordovician metamorphic basement and overlying Devonian and younger sedimentary successions, with absence of the Permian and Triassic strata (Fig. 1b). The metamorphic basement predominantly outcrops in the central part (Fig. 1b) and is composed of paragneiss, orthogneiss, migmatite, schist, quartzite and marble, denoting amphibolite facies and locally granulite facies metamorphism (Lin et al., 2008; Wang et al., 2012; 2013b). Paragneiss contains detrital zircons from 2.77 to 0.8 Ga, suggesting their deposition in the late Neoproterozoic (~800 Ma) (Wang et al., 2007a; 2013b; Wan et al., 2010).

The Yunkai domain underwent two major magmatic-metamorphic events, the first during the Early Paleozoic (440–420 Ma; Wang et al., 2007a; 2011; 2013b; Wan et al., 2010) and then in the Triassic (250–230 Ma; Wang et al., 2012; Chen et al., 2017). The Early Paleozoic igneous rocks in the Yunkai domain are predominantly gneissic granites (452–415 Ma) with subordinate massive gabbro and I-type granite (Fig. 1b; Wang et al., 2007a; Yu et al., 2018). Some Early Paleozoic granulite enclaves in the charnockite indicate peak metamorphism at T = 807–836 °C and P = 6.0–6.9 kbar based on garnet-orthopyroxene thermometry and garnet-plagioclase-orthopyroxene-quartz barometry (Chen and Zhuang, 1994). The Triassic igneous rocks mainly consist of massive garnet- and cordierite-bearing, strongly peraluminous granites with minor gneissic granites (251–224 Ma; Wang et al., 2013a; Chen et al., 2017). The peraluminous charnockites near the Yunkai domain contain cordierite and orthopyroxene, which crystallized at low temperatures (750–790 °C; Ti-in-biotite thermometer) and pressures (<3 kbar) (Zhao et al., 2017b). The Triassic thermal events also impacted the nearby Darongshan domain, where granulite enclaves in the Triassic peraluminous granite show metamorphic peak temperatures of 910–950 °C and peak pressures of 5.0–6.8 kbar estimated via phase relation forward modeling using the Perple_X (Zhao et al., 2017a). Some migmatite domes were developed in the Yunkai domain during the Early Paleozoic (438–435Ma; Chen et al., 2012; Wang et al., 2013b) and Triassic (~230 Ma), respectively, together with high-grade metamorphism and felsic magmatism (Wang et al., 2007b, 2012).

<Fig. 2>

Rock types

The studied migmatites are well exposed in a quarry in the Jindong area in the northwestern Yunkai domain (Fig. 1b). Most parts of the Jindong migmatites preserve pre-partial melting gneissic structure, shown by discontinuous foliated biotite layers alternating with leucocratic layers that are composed of quartz, K-feldspar and plagioclase (Fig. 2a), which defines the paleosome, following the classification of Sawyer (2008). Neosomes formed during anatexis contain biotite-poor granitic leucosomes (melt-rich parts) and biotite-rich melanosomes (residuum) (Fig. 2b). The Jindong migmatite may be classified as metatexite since leucosomes generally constitute about 15–20% of the Jindong migmatite (Fig. 2a). Melanosome in the Jindong migmatite shows gneissic structure, similar to the paleosome. Leucosome may be subdivided into lenticular and net-structured types that have different orientations (Fig. 2a). The lenticular leucosomes have lengths up to about 30 cm and thicknesses up to about 5 cm, and are generally subparallel to the foliation of biotite (Fig. 2a). The lenticular leucosomes tend to feed into felsic veins, forming net-structured leucosomes, which are discordant with the foliation and show variable thickness (10–20 cm) and length (>50 cm) (Fig. 2a, 2d, 2e). Some leucosome lenses contain biotite relicts captured from the biotite-rich melanosome (Fig. 2a, 2b; Fig. S2d). Samples collected in this study include melanosome (n = 10), lenticular leucosome (n = 8) and net-structured leucosome (n = 9).

The melanosome contains variable proportions of biotite (Bt, 11–24%), muscovite (Ms, 0.5–11%), plagioclase (Pl, 33–42%), K-feldspar (Kfs, 0.5–11%) and quartz (Qz, 33–40%) (Figs. 3, 4; Table A1) with accessory minerals of zircon (Zrn), apatite (Ap), monazite (Mnz), xenotime (Xtm) and ilmenite (Ilm) (Fig. 4e, 4f). Plagioclase and K-feldspar are anhedral, and some grains were resorbed with crystallization of albite and quartz in the margin (Figs. 3c, 4a, 4b). Some coarse-grained K-feldspars (1–5 cm in diameter) are enveloped by biotite (Fig. 2a). Biotite is fine grained and anhedral, and some crystals were resorbed and occur as relicts in albite (Fig. 4b). Muscovite is anhedral and shows straight contact with biotite and plagioclase (Fig.3d), with some crystals corroded in the margin (Fig. 4d). Apatite is abundant with variable grain size from 10 to 500 μm (Fig. 4e, 4f). Monazite and xenotime have grain sizes varying from 10 to 100 μm, and some grains occur as irregular rims surrounding apatite (Fig. 4e-f).

Lenticular leucosome is composed of muscovite (5–11%), K-feldspar (22–46%), plagioclase (11–19%) and quartz (29–56%) with minor biotite (2–5%) and accessory minerals, including ilmenite, zircon, apatite, monazite and xenotime (Fig. 3e-f). Biotite is broken with corroded margin (Fig. 3e). Muscovite is mostly fine grained and anhedral (Fig. 3e, f). Plagioclase occurs as irregular and elongated crystals (Fig. 3e-f). K-feldspar and quartz mainly occur as intergranular phases between other minerals (Fig. 3f).

Similar to the lenticular leucosomes, the net-structured leucosome contains predominant muscovite (5–10%), K-feldspar (20–38%), plagioclase (16–28%) and quartz (35–42%) with minor biotite (1–4%) (Fig. 3g) and accessory minerals of ilmenite, zircon, apatite, monazite and xenotime. Biotite is anhedral and mostly altered (Fig. 3f). Muscovite has straight boundaries with K-feldspar and plagioclase (Fig. 3g), indicating its magmatic origin. Plagioclase, K-feldspar and quartz are anhedral (Fig. 3g). Some plagioclase and quartz occur as round inclusions in K-feldspar.

<Fig. 3 & 4>

ANALYTICAL METHODS

Large melanosome samples (>1−3 kg) were collected and the coarse-grained K-feldspar (>0.5 cm) and leucosome lenses (length >1 cm) were cut off before crushing into powder, minimizing the compositional heterogeneity (Fig. S2a). The selected net-structured leucosomes (>1 kg) and lenticular leucosomes (thickness >3 cm; length >8 cm) were cut into small pieces before crushing into powder, and the entrained biotite-rich residuum in these leucosome samples were cut off to minimize contamination of mafic residuum (Fig. S2). The whole-rock major and trace elements and Nd isotope of samples in this study were analyzed at the Guizhou Tongwei Analytical Technology Co., Ltd.

Zircons and apatite were separated from the representative samples and embedded in epoxy mounts, which then were polished to expose the mineral center for imaging by cathodoluminescence (CL). *In situ* zircon U-Pb age and trace elements analyses were conducted at the Key Laboratory of Mineralogy and Metallogeny (KLMM), Guangzhou Institute of Geochemistry, Chinese Academy of Sciences (GIG-CAS). *In situ* apatite Nd isotope analyses were conducted at the State Key Laboratory of Isotope Geochemistry (SKLaBIG), GIG-CAS. Thin sections from representative melansome and leucosome samples were selected after detailed petrographic observations for back-scattered-electron (BSE) images and X-ray element mapping, and *in situ* mineral major and trace elements at the SKLaBIG, GIG-CAS. Detailed analytical procedures, supplemental figures (S1-S8) and tables (Table A1-A9) are compiled in the supplemental files.

ZIRCON U-PB AGE

Melanosome (sample YK17-56)

Zircons from this sample are prismatic crystals (150−200 μm). Most grains show oscillatory zoning and some zircons have thin dark rims in CL images (Fig. 5a). The analyzed zircons contain variable abundances of Th (30.8−164 ppm) and U (88−544 ppm) with Th/U from 0.11 to 1.27, indicating a magmatic origin (Table A2). They show enrichment of HREE (Yb = 205−1163 ppm; $[La/Yb]_N < 0.0002$) on chondrite-normalized patterns (Fig. S3a). Spots 09, 18 and 28 show old $^{206}Pb/^{238}U$ ages from 477±6 Ma to 749±8 Ma (Fig. 5c), which were interpreted to represent inherited zircon cores based on interpretation of the texture in CL images (Fig. 5a). The remaining twenty-six zircons show $^{206}Pb/^{238}U$ ages ranging from 431±3 Ma to 442±5 Ma (Table A2), yielding a

DOI: https://doi.org/10.2138/am-2022-8594. http://www.minsocam.org/

weighted mean age of 437±2 Ma (MSWD = 0.83; Fig. 5a), which is interpreted to represent the crystallization age of the igneous protolith.

Net-structured leucosome (sample YK17-59)

Zircons from this sample are prismatic crystals and 150−200 μm long. Most zircons show core-rim structure with bright cores and dark rims on CL images (Fig. 5c). The cores mostly show oscillatory zoning and have variable HREE (e.g., Yb = 152−2433 ppm), Th (52.7−278 ppm) and U (148−2093 ppm) contents with Th/U ratios of 0.06 to 0.89. They gave $^{206}Pb/^{238}U$ ages from 431±3 to 755±10 Ma and were interpreted as zircons inherited from the protolith. The 22 analyses on rims yielded a weighted mean $^{206}Pb/^{238}U$ age of 238±1 Ma (MSWD = 0.79; Fig. 5d), which is interpreted to represent the crystallization age of leucosome. The dark rims show variable HREE (Yb = 140−1991 ppm), Th (9.43−969 ppm) and U (494−3132 ppm) contents with Th/U ranging from 0.01 to 0.59 (Fig. S3b; Table A2).

<Fig. 5>

WHOLE-ROCK GEOCHEMISTRY

Whole-rock major and trace elements and Nd isotopes for the Jindong melanosome and leucosome are shown in Figs. 6 and 7, and listed in Tables A3 and A4. Melanosome samples contain variable SiO_2 (66.4–71.1 wt%), MgO (0.91–1.82 wt%), Fe_2O_3 (3.32–6.59 wt%), TiO_2 (0.42–0.88 wt%), Na_2O (2.80–3.24 wt%) and K_2O (2.06–4.02 wt%) (Fig. 6). They show chondrite normalized LREE-enriched patterns ($[La/Yb]_N$ = 3.20–16.9) with moderately negative Eu anomalies (Eu/Eu^* = 0.25–0.49; Fig. 7a). On the primitive mantle-normalized multi-element spidergram, these samples are characterized by

This is the peer-reviewed, final accepted version for American Mineralogist, published by the Mineralogical Society of America.
The published version is subject to change. Cite as Authors (Year) Title. American Mineralogist, in press.
DOI: https://doi.org/10.2138/am-2022-8594. http://www.minsocam.org/

negative Sr-Ba-Nb-Ti and positive Pb anomalies (Fig. 7b). They show low $^{143}Nd/^{144}Nd$ (0.512009–0.512159) ratios with negative whole-rock $\varepsilon_{Nd}(t)$ values (-10.2 to -7.2; t = 238 Ma; Table A4).

The lenticular leucosome samples contain higher SiO_2 (71.2–80.8 wt%) and K_2O (4.50–8.15 wt%) and much lower MgO (0.07–0.36 wt%), TiO_2 (0.03–0.16 wt%) and Fe_2O_3 (1.14–1.50 wt%) than the melanosome samples (Fig. 6). These samples have variable Na_2O (1.38–2.38 wt%), Rb (166–258 ppm), Ba (521–2130 ppm), Sr (50.4–131 ppm) and REE contents (43.4–184 ppm) with LREE-enriched chondrite normalized patterns ($[La/Yb]_N$ = 1.72–7.02) and weakly positive to negative Eu anomalies (Eu/Eu^* = 0.40–1.11; Fig. 7; Table A3). They show variable $^{143}Nd/^{144}Nd$ ratios (0.511886–0.512136), corresponding to $\varepsilon_{Nd}(t)$ values of -13.1 to -8.6 (t = 238 Ma; Table A4).

The net-structured leucosome samples show similarly low MgO (0.11–0.26 wt%), TiO_2 (0.08–0.16 wt%) and Fe_2O_3 (0.70–1.32 wt%) abundances with the lenticular leucosome samples, and have slightly higher Na_2O (2.04–3.15 wt%) and lower Ba (56.3–1120 ppm) and Sr (6.36–66.1 ppm) contents (Figs. 6, 7). They have variable REE contents (44.6–119 ppm) and show slightly enriched chondrite normalized LREE ($[La/Yb]_N$ = 1.21–2.85) patterns with negative Eu anomalies (Eu/Eu^* = 0.17–0.71; Fig. 7). These samples exhibit positive U and Pb, and negative Nb-Ti anomalies on the spidergram (Fig. 7b). They have variable $^{143}Nd/^{144}Nd$ ratios (0.512033–0.512079) with negative whole-rock $\varepsilon_{Nd}(t)$ values from -11.4 to -9.3 (t = 238 Ma; Table A4).

<Fig. 6 & 7>

MINERAL GEOCHEMISTRY

Mineral compositions for biotite, muscovite, plagioclase and K-feldspar, zircon and apatite from the melanosome, lenticular leucosome and net-structured leucosome are listed in Tables A5 (major elements) and A6 (trace elements), and shown in Figs. 8, S3–S5. Apatite Nd isotope data are presented in Table A7.

Biotite

Biotite in the melanosome samples shows low $Mg^{\#}$ values (0.33–0.35), and has variable Ti (0.25-0.44 apfu), Rb (1013–1116 ppm), Ba (328–640 ppm) and Nb (102–125 ppm), and lower Sr (0.52–3.02 ppm), Th (<0.17 ppm) and REE (mostly <0.65 ppm) contents (Fig. 8a; Table A6). Biotite in the net-structured leucosome has been mostly altered to chlorite and could not be analyzed (Fig. 3g). On the other hand, biotite in the lenticular leucosome samples show similar major and trace elemental compositions with those in the melanosome (Fig. S4a). It has low $Mg^{\#}$ values (0.33–0.35) and shows variable Ti (0.23-0.44 apfu), Rb (998–1212 ppm), Ba (253–500 ppm) and Nb (106–137 ppm) with low Sr (0.24–0.55 ppm), Th (<0.11 ppm) and REE (mostly <1.63 ppm) concentrations (Fig. 8a; Table A6).

Muscovite

Muscovite in the melanosome has variable Mg (0.20–0.76 apfu) (Fig. S4b) and contains high Rb (533–575 ppm), Ba (831–994 ppm) and Nb (81.6–105 ppm) with low Sr (5.17–7.02 ppm), Th (<0.66 ppm), U (<1.89 ppm) and REE (0.78–31.0 ppm) contents (Fig. 8b; Table A6). Muscovite in the lenticular leucosome has a narrow range of Mg (0.20–0.28 apfu), Rb (520–581 ppm) and Sr (4.95–6.01 ppm) and contains lower Ba (594–771 ppm) contents than those in the melanosome (Figs. 8b; Table A6). Muscovite in the net-structured leucosome has lower Mg (0.07–0.11 apfu), Ba (3.61–18.5 ppm) and Sr (0.22–0.90 ppm) and higher Rb (870–1029 ppm) and Nb (110–160 ppm) contents than those in melanosome and lenticular leucosome samples (Fig. 8b; Table A6).

Plagioclase

Plagioclase in the melanosome is An = 22–40 (Fig. S4c) and has variable contents of Sr (109–503 ppm), Ba (36.9–419 ppm), Rb (0.10–30.9 ppm) and REE (5.75−38.6 ppm) (Fig. 8c; Table A6). Some plagioclase grains occur along the margin of biotite and K-feldspar (Fig. 4b, 4c, 4d) and are mainly albite (An = 2–26) (Pl-B in Fig. S4c).

Plagioclase in lenticular leucosome is An = 20–30 (Fig. S4c), and has overall lower REE (1.76−25.0 ppm), Sr (197–227 ppm) and Ba (11.5–47.7 ppm) abundances than those in the melanosome (Fig. 8c; Table A6). Plagioclase in the net-structured leucosome is mainly albite (An = 1−12; Fig. S4c) and contains lower contents of Sr (15.5–22.4 ppm) and Ba (0.12–4.02 ppm) than those in lenticular leucosome and melanosome (Fig. 8c; Table A6).

K-feldspar

K-feldspar in the melanosome has high orthoclase (Or) content (typically 92–98; Table A5) and contains high Rb (411–438 ppm), Ba (3465–4160 ppm) and low Sr (137–202 ppm) and REE (4.12–5.41 ppm) contents (Fig. 8d; Table A6). K-feldspar in the lenticular leucosome has variable orthoclase (Or) content (mainly 84–98; Table A5) and contains Rb (325–457 ppm) and Sr (126–182 ppm) contents similar to those in melanosome, but with lower Ba (1656–2207 ppm) contents (Fig. 8d; Table A6). K-feldspar in the net-structured leucosome has orthoclase content (Or = 92–99) similar to those in the melanosome and the lenticular leucosome, but possesses higher Rb (809–

1039 ppm) and lower Ba (51.7–264 ppm) and Sr (16.2–51.1 ppm) contents (Fig. 8d; Table A6).

Apatite

Apatite in the melanosome has high Y (2300–3355 ppm), REE (3657–5213 ppm) and U (15.4–39.5 ppm) and has relatively low Th contents (2.67–8.50 ppm) and low Th/U ratios (0.17–0.24; Table A6). It shows inverted U-shaped chondrite-normalized REE patterns that are characterized by lower LREE and HREE contents than MREE with low $[La/Sm]_N$ (0.42–0.49) and $[La/Yb]_N$ (0.83–0.89) values and strongly negative Eu anomaly (Eu/Eu^* = 0.07–0.08; Fig. S5). Apatite has high $^{147}Sm/^{144}Nd$ (0.30198±9 to 0.31895±8) and low $^{143}Nd/^{144}Nd$ ratios (0.512125±25 to 0.512206±23) with negative $\varepsilon_{Nd}(t)$ values (-13.2 to -11.9; t = 238 Ma; Table A7).

<Fig. 8>

DISCUSSION

Triassic anatexis of Early Paleozoic gneissic granite

The Yunkai domain underwent multi-stage crustal anatexis with development of voluminous granites in the Early Paleozoic, Late Permian-Triassic and Jurassic-Cretaceous (Fig. 1; Wang et al., 2013a; Chen et al., 2017). Zircons from the Jindong melanosome samples yield a crystallization age of 437±2 Ma (Fig. 5b), indicating that the protolith of the Jindong migmatite was emplaced during the Early Paleozoic, coeval with regional magmatism (452–415 Ma; Wang et al., 2011; Chen et al., 2012; Yu et al., 2019). On the other hand, the net-structured leucosomes contain two groups of zircons with different ages (Fig. 5d). The older zircons show $^{206}Pb/^{238}U$ ages from 431±3 to 755±10 Ma (Fig. 5d), similar to zircons from the melanosome, indicating their inheritance from the protolith. The younger population of zircons yielded a mean $^{206}Pb/^{238}U$ age of 238±1 Ma with Th/U ratios > 0.1 (Table A2), denoting their crystallization from magmas (Hoskin and Schaltegger, 2003). These zircons are coeval with the Triassic high-grade metamorphism and migmatization (260–230 Ma; Wang et al., 2007b, 2012) and felsic magmatism (250–224 Ma; Chen et al., 2017) in the Yunkai domain. The Jindong melanosomes generally preserve the gneissic structure of the paleosome (Fig. 2), as defined by oriented biotite and feldspar minerals (Figs. 2, 3c). In contrast, lenticular and net-structured leucosomes lack preferred orientation of minerals (Fig. 3f, g), suggesting that deformation is predominantly Early Paleozoic in age as determined for other gneissic granites in the Yunkai domain (Yu et al., 2018). Thus, geochronology and petrographic features suggest that the Jindong migmatite was possibly formed during the Triassic crustal anatexis with melting of the Early Paleozoic gneissic granite.

Melting process of the Jindong migmatite

Granitic melts may be generated by water-fluxed partial melting in the deep crust, or by dehydration melting process, respectively (Weinberg and Hasalová, 2015). It has been suggested that migmatites in the Yunkai domain formed mainly through dehydration melting process as a result of the following reactions: Ms + Pl + Qz → Sil + Kfs + melt, Bt + Qz + Pl → Opx +Kfs + melt, or Bt + Qz + Pl + Sil → Grt + Kfs + melt (Wang et al., 2013b). Recent studies also suggest that some migmatites may be products of water-fluxed melting process, due to the absence of peritectic minerals in the melanosome (Yu et al. 2019).

Biotite in the Jindong leucosome has similar major and trace element compositions to those in the melanosome (Figs. 8a; S4a), suggesting that it is a relict captured from the melanosome rather than a peritectic mineral (Fig. 3b). Biotite and muscovite in the melanosome show corroded margins (Figs. 3c, 4b, 4d), indicating that they may have partly broken down in the melt without producing peritectic minerals, in a possible congruent melting reaction. Furthermore, K-feldspar and plagioclase in the melanosome samples show embayed margins (Fig. 4a, 4b), illustrating consumption of these minerals during melting. The absence of anhydrous peritectic minerals during melting of biotite and breakdown of feldspars are all consistent with a water-fluxed melting process defined by the congruent melting reaction: Bi + Ms + Pl + Kfs + Qz + H_2O → melt (Eq.1).

Change of melt composition by melt segregation

The Jindong leucosomes exhibit variations in both major and trace elements (Fig. 6), which should be the result of a combination of the initial melt composition, proportional to the mineral phases in the melting reaction (Eq. 1), and modification during melt migration process (Chappell et al., 1987; White and Powell, 2010; Brown et al., 2016; Wolfram et al., 2017). The Jindong leucosomes exhibit variable K_2O contents that may reflect breakdown of K-feldspar in different proportions during melting (Fig. 6a). On the other hand, the net-structured leucosomes in the Jindong migmatites are fed by the lenticular leucosomes, which records the melt segregation process (Fig. 2a). Muscovite, plagioclase and K-feldspar in net-structured and lenticular leucosomes show distinct compositions (Fig. 8), suggesting change of melt compositions during the

DOI: https://doi.org/10.2138/am-2022-8594. http://www.minsocam.org/

segregation process. Low TiO_2, Fe_2O_3 and MgO contents of the Jindong leucosomes suggest that entrainment of minerals from melanosome should not be the major mechanism for the change of melt compositions (Fig. 6). It should be noted that the plagioclase in net-structured leucosomes has lower An (1−12) than those in lenticular leucosomes (An = 20–30; Fig. S4c), suggesting that the net-structured leucosome may represent evolved products fractionated from the lenticular leucosomes. Thus, minerals in net-structured leucosomes show higher Rb and much lower Ba and Sr contents than those in lenticular leucosomes (Fig. 8), implying elevation of Rb and decreasing Ba and Sr in melts during the segregation.

In felsic magmatic systems, Ba and Sr are mainly hosted in K-feldspar and plagioclase, respectively, while Rb is incompatible in both minerals (Bacon and Druitt, 1988; Stix and Gorton, 1990; Ewart and Griffin, 1994). Early fractionation of these minerals will lower Ba and Sr and increase Rb in the residual melts (Fig. 9), which may explain fractionation of Rb, Sr and Ba during the melt segregation. To evaluate the influence of fractional crystallization on composition of melts, we calculated the fractional crystallization of K-feldspar and plagioclase in different proportions (Fig. 9). Sample YK17-58b is selected as starting material because this sample has higher Ba and Sr than other leucosome samples (Fig. 9; Table A3), suggesting that its composition experienced less modification by fractional crystallization. The Jindong leucosome samples mainly plot along the compositional evolution trend of fractional crystallization of K-feldspar and plagioclase, reflecting early fractionation of feldspars during melt migration (Fig. 9).

<Fig. 9>

Accessory minerals controlling REE and Nd isotope in granitic melts

Variations of REE, Th and Y. The leucosome samples show variable REE, Y and Th (Fig. 7), and have low TiO_2, Fe_2O_3 and MgO contents (Fig. 6), indicating that the compositional variations are not caused by entrainment of mafic residuum (Fig. S6). Further to that, the Jindong leucosomes show poor correlation between LREE and Yb with Rb/Sr ratios (Fig. S6), excluding early fractionation of feldspars as an explanation for the changing REE content of melts. This is consistent with high incompatibility of REE, Y and Th in plagioclase and K-feldspar (Bea et al. 1994; Ewart and Griffin 1994). Thus, variable REE, Y and Th contents in these samples should be attributed to the melting process.

The key problem for modeling the contributions of different mineral phases in a source through to the budget of REE, Y and Th in melts is constraining the composition of the initial melt. We have argued above that the fractional crystallization process during melt segregation made insignificant modifications to the REE, Y and Th contents of the melts (Fig. S6), suggesting that the Jindong leucosomes may preserve similar REE, Y and Th element abundance as the initial melts. On the other hand, the melting reactions involving Pl-Kfs-Qz and small proportions of Bt-Ms in the presence of H_2O would produce melts that are poor in REE, Y and Th. For example, by employing average major element compositions of minerals in the melanosome, we can model a possible melting reaction of 0.033Bt + 0.01Ms + 0.347Qz + 0.41Kfs + 0.20Pl = 1 melt (Eq. 2), which produces a melt similar to the average composition of the lenticular leucosome (Fig. 6). The melt will only account for ~8% REE, ~2% Y, and ~0.37% Th in the leucosome

This is the peer-reviewed, final accepted version for American Mineralogist, published by the Mineralogical Society of America.
The published version is subject to change. Cite as Authors (Year) Title. American Mineralogist, in press.
DOI: https://doi.org/10.2138/am-2022-8594. http://www.minsocam.org/

samples (Fig. 10a), because of the low content of these elements in major mineral phases (Table A6). We therefore focus on the fate of accessory phases, such as zircon (Y and HREE), monazite (Th and LREE), xenotime (Y and HREE) and apatite (REE) (Bea, 1996; Ayres and Harris, 1997; Zeng et al., 2005; Schwindinger et al., 2020).

Zircons in the Jindong melanosomes show variable content of Y (593–3386 ppm) and HREE (Yb = 205–1163 ppm) and may account for ~2% Y and ~9% Yb of the total whole-rock content (Fig. S7; Table A9). The Jindong leucosomes show a wide range of Zr contents (40–138 ppm) (Fig. 7b). Based on the melting reaction (Eq. 2), the breakdown of the rock-forming minerals may contribute about ~16% of whole-rock Zr content in the leucosome samples (Fig. 10b; Table A8). This suggests that ~84% of whole-rock Zr content in leucosome samples came from dissolution or entrainment of zircon from melanosome. Since REE content is much lower than Zr in zircon (Zr/Y = 144–840; Zr/Yb = 410–2424; Table A6), the dissolved or entrained zircons from melanosome may only contribute ~ 1% Y and 4% Yb of in the Jindong leucosomes (Fig. 10b; Table A8). This indicates that zircon dissolution or entrainment was an insignificant contributor to REE budgets in the granitic melts.

Bea (1996) suggested that >80% REE and Th in crustal rocks may reside in phosphates, including apatite, monazite and xenotime, and dissolution of these minerals during melting may determine REE and Th concentrations in granitic melts. The Jindong leucosomes show variable La, Yb, Th and Y abundances, which tend to decrease with increasing P_2O_5 content (Fig. 11). This is contrast with the dissolution of phosphate that increases abundance of these elements in melts (e.g., Wolf and London, 1995; Bea, 1996). Dissolution of phosphate minerals, including apatite, monazite and xenotime, in granitic

This is the peer-reviewed, final accepted version for American Mineralogist, published by the Mineralogical Society of America.
The published version is subject to change. Cite as Authors (Year) Title. American Mineralogist, in press.
DOI: https://doi.org/10.2138/am-2022-8594. http://www.minsocam.org/

melts is influenced by pressure, temperature and melt composition (Montel et al., 1993; Wolf and London, 1995). In general, apatite is dissolved more efficiently in strongly peraluminous melts at higher temperature, rising by a factor of 10 as melt ASI (aluminum saturation index) values increase from 1.1 to 1.2 (Wolf and London, 1995), while monazite and xenotime tend to show low solubility in peraluminous melt and become saturated at low P_2O_5 (e.g., ≤0.05 wt%; Montel et al., 1993; Wolf and London, 1995). The Jindong leucosomes are all peraluminous (A/CNK = 1.04–1.17), which favors apatite dissolution. However, modeling results reveal that dissolution of apatite only accounts for ~9% REE, ~16% Y and ~0.02 % Th of whole-rock budget in leucosome (Fig. 10c; Table A8). This indicates that the majority of REE, Th and Y of the Jindong leucosomes may be derived from the dissolution of other phosphates, such as monazite and xenotime, in the source (Fig. 11), which contain extremely high abundances of REE (a factor of 100–1000 higher than apatite; Bea, 1996).

Continuous dissolution of apatite in the peraluminous melts may cause oversaturation of monazite and xenotime with respect to phosphorus (Wolf and London, 1995; Wolfram et al., 2017; Schwindinger et al., 2020). In the melanosome samples, the rounded apatite grains are commonly surrounded by irregular rims of monazite and xenotime (Fig. 4e, f), demonstrating dissolution of apatite with precipitation of monazite/xenotime, as shown by reaction of apatite + melt-1 → monazite /xenotime + melt-2 (Eq. 3; Wolf and London, 1995). Because Th, REE and Y are more compatible in monazite and xenotime than in apatite, the dissolution of apatite with precipitation of monazite and xenotime results in decreasing REE, Th and Y with increasing P_2O_5 in the melts (Fig. 11). The impact of this process can be observed in the Jindong leucosomes that define a very sharp decrease for REE, Th and Y with slightly increasing of P_2O_5 content (Fig. 11). Thus, the variability of these elements in the leucosomes may be ascribed to the saturation and removal of monazite and xenotime from melt with minimal impact on P_2O_5 content due to dissolution of apatite (Fig. 11).

<Fig. 10 & 11>

Variation of Nd isotope. Some authors suggest that Nd isotopic compositions of granitic melts are mainly controlled by the dissolution of LREE-enriched accessory minerals, such as apatite and monazite (Ayres and Harris, 1997; Zeng et al., 2005; Korhonen et al., 2010b). We note that >88 % of Nd in melanosome samples is hosted by monazite, while apatite has low Nd abundances, accounting for only 9%, and rock-forming minerals and zircon account for approximately 3% and 0.001% of Nd in the melanosome, respectively (Fig. S7; Table A9). Therefore, the whole-rock Nd isotope of these melanosome samples ($\varepsilon_{Nd}(t)$ = -10.2 to -7.2; t = 238 Ma) should reflect the Nd isotopes of monazite. On the other hand, the Jindong leucosomes show variable $\varepsilon_{Nd}(t)$ values (-8.6 to -13.1; Fig. 12). A number of leucosome samples exhibit similar $\varepsilon_{Nd}(t)$ values to those for the melanosomes (Fig. 12b), consistent with inheritance of their Nd from the breakdown of monazite in their sources. Meanwhile, other samples show lower $\varepsilon_{Nd}(t)$ values than the melanosome, implying influence of other Nd-bearing minerals (e.g., apatite) on the Nd isotope of granitic melts (Zeng et al., 2005).

Differences in isotopic composition between different minerals may occur even in high-temperature granites and high-grade metamorphic rocks (e.g., Farina et al., 2014). For example, apatite in the Jindong melanosome has much lower ε_{Nd}(437Ma) values

DOI: https://doi.org/10.2138/am-2022-8594. http://www.minsocam.org/

(-16.1 to -14.6) than the whole-rock (-7.8 to -5.8; Fig. 12a), illustrating isotopic disequilibrium between the minerals during emplacement of protolith (e.g., Xu et al., 2015). These initial differences in isotopic composition at 437 Ma would remain at the time of anatexis (~238 Ma) when apatite would have lower $\varepsilon_{Nd}(t)$ values (-13.2 to -11.9) than the whole-rock (-9.8 to -7.4; Fig. 12a). Three leucosome samples have $\varepsilon_{Nd}(t)$ values that are lower than the source, and show relatively high P_2O_5 contents, suggesting that their Nd isotopes may be influenced by dissolution of the low $\varepsilon_{Nd}(t)$ apatite (Fig. 12b). Precipitation of monazite would decrease Nd in residual melts and may also account for the relatively low Nd contents of the three leucosome samples (Fig. 12c). Thus, continuous dissolution of apatite during anatexis increases P_2O_5 contents of the melt while causes the decrease in $\varepsilon_{Nd}(t)$ values (Fig. 12b).

We therefore conclude that Nd isotope of the Jindong leucosome are controlled by a combination of monazite and apatite dissolution. At the initial stage of melting, both monazite and apatite will be dissolved in melts at low P_2O_5 content (e.g., < ~0.05 wt%). Since monazite have much higher Nd content than apatite, Nd isotope of melts should be dominated by dissolution of monazite (Fig. 12; Wolf and London, 1995). Alternatively, when monazite was a peritectic phase after apatite breakdown, with increasing P_2O_5 content (e.g., > ~0.05 wt%) in melts, the Nd isotopic signature of the melts would be controlled by the continuous dissolution of apatite, which would decrease their $\varepsilon_{Nd}(t)$ values (Fig. 12).

<Fig. 12>

IMPLICATIONS FOR PETROGENESIS OF GRANITE

This is the peer-reviewed, final accepted version for American Mineralogist, published by the Mineralogical Society of America.
The published version is subject to change. Cite as Authors (Year) Title. American Mineralogist, in press.
DOI: https://doi.org/10.2138/am-2022-8594. http://www.minsocam.org/

Rb, Sr and Ba fractionation during crustal anatexis

The Jindong leucosomes exhibit variable contents of Rb, Sr and Ba and show negative correlation between Rb/Sr and Ba (Fig. 9). This trend has been used to distinguish between granites formed through melting processes with or without water (Fig. 9c; Zhang et al., 2004; Gao et al., 2017). However, this study suggests that fractional crystallization of feldspars during melt segregation may cause significant fractionation of Rb, Sr and Ba, resembling dehydration melting process (Fig. 9; Fig. 13). This demonstrates the significance of melt segregation in modifying the composition of granitic melts.

Importance of accessory minerals in controlling REE and Nd isotope of granite

REE contents of granites have been widely used to constrain melting processes (e.g., Moyen, 2009 and the references therein). For example, low HREE and high La/Yb ratio of granitic melts could reflect residual garnet during melting at high pressure, such as formation of granites with adakitic features (Le Breton and Thompson, 1988; Wyllie and Wolf, 1993; Wolf and Wyllie, 1994; Wang et al., 2008; Moyen, 2009). The Jindong leucosomes exhibit variable REE content in the absence of garnet in the system, and it is likely due to dissolution of apatite, xenotime and monazite in different proportions (Figs. 11, 12, 13). This demonstrates the importance of accessory minerals in controlling REE (except Eu) contents of granitic melts (Bea, 1996; Ayres and Harris, 1997). In fact, P_2O_5 of the Tibetan adakites negatively correlate with $\varepsilon_{Nd}(t)$ values and positively correlate with La and Yb (Figs. 11, S1d), indicating that their REE contents could also be influenced by dissolution of phosphates, in addition to garnet. In addition, the Jindong leucosomes tend to show lower REE contents and $\varepsilon_{Nd}(t)$ values as increasing P_2O_5

content, due to the dissolution of apatite with precipitation of monazite and xenotime (Figs. 11, 12, 13). We compiled compositional data from granites worldwide, such as those from the South China Block, Tasman Orogen and Himalayan area, which show similar compositional and isotopic patterns to the Jindong leucosome in this study (Figs. 11, S1, S8). Therefore, we suggest that the strong controls of accessory phases on REE geochemistry and Nd isotope is common in petrogenesis of granite.

<Fig. 13>

Acknowledgements

We thank S.L. Sun, J.L. Ma and X.L. Tu for analytical assistance. This study was financially supported by the National Natural Science Foundation of China (NSFC Projects 41902056, 42021002, 41625007) and the Key Special Project for Introduced Talents Team of Southern Marine Science and Engineering Guangdong Laboratory (Guangzhou) (GML2019ZD0202). This is contribution No. IS-XXXX from GIG-CAS.

References Cited

Ayres, M., and Harris, N. (1997) REE fractionation and Nd-isotope disequilibrium during crustal anatexis: constraints from Himalayan leucogranites. Chemical Geology, 139, 249–269.

Bacon, C.R., and Druitt, T.H. (1988) Compositional Evolution of the Zoned Calcalkaline Magma Chamber of Mount-Mazama, Crater Lake, Oregon. Contributions to Mineralogy and Petrology, 98(2), 224–256.

Bea, F. (1996) Residence of REE, Y, Th and U in granites and crustal protoliths: Implications for the chemistry of crustal melts. Journal of Petrology, 37, 521–552.

Bea, F., Pereira, M.D., and Stroh, A. (1994) Mineral/leucosome trace-element partitioning in a peraluminous migmatite (a laser ablation-ICP-MS study). Chemical Geology, 117, 291–312.

Brown, M. (2013) Granite: from genesis to emplacement. Geological Society of America Bulletin, 125, 1079–1113.

Brown, C.R., Yakymchuk, C., Brown, M., Fanning, C.M., Korhonen, F.J., Piccoli, P.M., and Siddoway, C.S. (2016) From Source to Sink: Petrogenesis of Cretaceous Anatectic Granites from the Fosdick Migmatite-Granite Complex, West Antarctica. Journal of Petrology, 57(7), 1241–1278.

Chappell, B.W., White, A.J.R., and Wyborn, D. (1987) The importance of residual source material (restite) in granite petrogenesis. Journal of Petrology, 28, 1111–1138.

Chen, B., and Huang, F.S. (1994) On the origin of migmatite in Yunlu, Western Guangdong Province. Acta Geologica Sinica, 68(3), 231–241 (in Chinese with English abstract).

Chen, B., and Zhuang, Y.X. (1994) The petrology and petrogenesis of Yunlu charnockite and its granulite inclusion, west Guangdong, South China. Acta Petrologica Sinica, 10, 139–149 (in Chinese with English abstract).

Chen, C.H., Liu, Y.H., Lee, C.Y., Xiang, H., and Zhou, H.W. (2012) Geochronology of granulite, charnockite and gneiss in the poly-metamorphosed Gaozhou Complex

(Yunkai massif), South China: emphasis on the in-situ EMP monazite dating. Lithos, 144–145, 109–129.

Chen, C.H., Liu, Y.H., Lee, C.Y., Sano, Y., Zhou, H.W., Xiang, H., and Takahata, N. (2017) The Triassic reworking of the Yunkai massif (South China): EMP monazite and U-Pb zircon geochronologic evidence. Tectonophysics, 694, 1–22.

Clemens, J.D., and Stevens, G. (2016) Melt segregation and magma interactions during crustal melting: Breaking out of the matrix. Earth-Sciences Review, 160, 333–349.

Clemens, J.D., Elburg, M.A., and Harris, C. (2017) Origins of microgranular igneous enclaves in granitic rocks: the example of Central Victoria, Australia. Contributions to Mineralogy and Petrology, 172, 88.

Clemens, J.D. (2018) Granitic magmas with I-type affinities, from mainly metasedimentary sources: the Harcourt batholith of southeastern Australia. Contributions to Mineralogy and Petrology, 173, 93.

Ewart, A., and Griffin, W.L. (1994) Application of Proton-Microprobe Data to Trace-Element Partitioning in Volcanic-Rocks. Chemical Geology, 117(1–4), 251–284.

Farina, F., and Stevens, G. (2011) Source controlled $^{87}Sr/^{86}Sr$ isotope variability in granitic magmas: the inevitable consequence of mineral-scale isotopic disequilibrium in the protolith. Lithos, 122, 189–200.

Farina, F., Dini, A., Rocchi, S., and Stevens, G. (2014) Extreme mineral-scale Sr isotope heterogeneity in granites by disequilibrium melting of the crust. Earth and Planetary Science Letters, 399, 103–115.

Gao, P., Zheng, Y.F., and Zhao, Z.F. (2017) Triassic granites in South China: A geochemical perspective on their characteristics, petrogenesis, and tectonic significance. Earth-Sciences Reviews, 173, 266–294.

Guo, Z.F., and Wilson, M. (2012) The Himalayan leucogranites: Constraints on the nature of their crustal source region and geodynamic setting. Gondwana Research, 22, 360–376.

Hergt, J., Woodhead, J., and Schofield, A. (2007) A-type magmatism in the Western Lachlan Fold Belt? A study of granites and rhyolites from the Grampians region, Western Victoria. Lithos, 97, 122–139.

Huang, X.L., Yu, Y., Li, J., Tong, L.X., and Chen, L.L. (2013) Geochronology and petrogenesis of the early Paleozoic I-type granite in the Taishan area, South China: middle-lower crustal melting during orogenic collapse. Lithos, 177, 268–284.

Hoskin, P.W., and Schaltegger, U. (2003) The composition of zircon and igneous and metamorphic petrogenesis. Reviews in Mineralogy and Geochemistry, 53, 27–62.

Iles, K.A., Hergt, J.M., Woodhead, J.D., Ickert, R.B., and Williams, L.S. (2020) Petrogenesis of granitoids from the Lachlan Fold Belt, southeastern Australia: The role of disequilibrium melting. Gondwana Research, 79, 87–109.

Kemp, A.I.S., and Hawkesworth, C.J. (2003) Granitic perspectives on the generation and secular evolution of the continental crust. Treatise of Geochemistry, 3, 1–64.

King, J., Harris, N., Argles, T., Parrish, R.R., and Zhang, H.F. (2011) Contribution of crustal anatexis to the tectonic evolution of Iia crust beneath southern Tibet. Geological Society of America Bulletin, 123, 218–239.

Koblinger, B.M., and Pattison, D.R.M. (2017) Crystallization of Heterogeneous Pelitic Migmatites: Insights from Thermodynamic Modelling. Journal of Petrology, 58(2), 297–326.

Korhonen, F.J., Saito, S., Brown, M., Siddoway, C.S., and Day, J.M.D. (2010) Multiple Generations of Granite in the Fosdick Mountains, Marie Byrd Land, West Antarctica: Implications for Polyphase Intracrustal Differentiation in a Continental Margin Setting. Journal of Petrology, 51(3), 627–670.

Kriegsman, L.M. (2001) Partial melting, partial melt extraction and partial back reaction in anatectic migmatites. Lithos, 56(1), 75–96.

Le Breton, N., and Thompson, A.B. (1988) Fluid-absent (dehydration) melting of biotite in metapelites in the early stages of crustal anatexis. Contributions to Mineralogy and Petrology, 99, 226–237.

Lin, W., Wang, Q.C., and Chen, K. (2008) Phanerozoic tectonics of south China block: new insights from the polyphase deformation in the Yunkai massif. Tectonics, 27, TC6004. http://dx.doi.org/10.1029/2007TC002207.

Liu, Z.C., Wu, F.Y., Ji, W.Q., Wang, J.G., and Liu, C.Z. (2014) Petrogenesis of the Ramba leucogranite in the Tethyan Himalaya and constraints on the channel flow model. Lithos, 208–209, 118–136.

Liu, Z.C., Wu, F.Y., Ding, L., Liu, X.C., Wang, J.G., and Ji, W.Q. (2016) Highly fractionated Late Eocene (~35 Ma) leucogranite in the Xiaru Dome, Tethyan Himalaya, South Tibet. Lithos, 240–243, 337–354.

McDonough, W.F., and Sun S.S. (1995) The composition of the Earth. Chemical Geology, 120, 223–253.

Montel, J.M. (1993) A model for monazite/melt equilibrium and the application to the generation of granitic magmas. Chemical Geology, 110, 127–146.

Moyen, J.F. (2009) High Sr/Y and La/Yb ratios: the meaning of the "adakitic signature". Lithos, 112, 556–574.

Rosenberg, C.L., and Handy, M.R. (2005) Experimental deformation of partially melted granite revisited: implications for the continental crust. Journal of Metamorphic Geology, 23, 19–28.

Rudnick, R.L., and Gao, S. (2003) Composition of the continental crust. Treatise of Geochemistry, 3, 1–64

Sawyer, E.W. (2001) Melt segregation in the continental crust: distribution and movement of melt in anatectic rocks. Journal of Metamorphic Geology, 19, 291–309.

Sawyer, E.W. (2008) Atlas of Migmatites. The Canadian Mineralogist, Special Publication 9. NRC Research Press, pp. 371.

Schwindinger, M., Weinberg, R.F., and White, R.W. (2020) The Fate of Accessory Minerals and Key Trace Elements During Anatexis and Magma Extraction. Journal of Petrology, 61 (2).

Singh, B., Kumar, S., Ban, M., and Nakashima, K. (2016) Mineralogy and geochemistry of granitoids from Kinnaur region, Himachal Higher Himalaya, India: Implication on the nature of felsic magmatism in the collision tectonics. Journal of Earth System Science, 125(7), 1329–1352.

Sun, S.S., and McDonough, W.F. (1989) Chemical and isotopic systematics of oceanic basalts: implication for mantle composition and process. In: Sauders, A.D., Norry, M.J. (Eds.), Magmatism in the ocean Basins. Geological Society Special Publications, 42, 313–345.

Stix, J., and Gorton, M.P. (1990) Variations in Trace-Element Partition-Coefficients in Sanidine in the Cerro Toledo Rhyolite, Jemez Mountains, New-Mexico - Effects of Composition, Temperature, and Volatiles. Geochimica et Cosmochimica Acta, 54(10), 2697–2708.

Vernon, R.H., Collins, W.J., and Richards, S.W. (2003) Contrasting magmas in metapelitic and metapsammitic migmatites in the Cooma Complex, Australia. Visual Geosciences, 8.

Visonà, D., and Lombardo, B. (2002) Two mica- and tourmaline leucogranites from the Everest-Makalu region (Nepal-Tibet). Himalayan leucogranite genesis by isobaric heating? Lithos, 62 (3–4), 125–150.

Wan, Y.S., Liu, D.Y., Simon, A.W., Cao, J.J., Chen, B., and Dong, C.Y. (2010) Evolution of the Yunkai Terrane, South China: Evidence from SHRIMP zircon U-Pb dating, geochemistry and Nd isotope. Journal of Asian Earth Sciences, 37, 140–153.

Wang, D., Zheng, J.P., Ma, Q., Griffin, W.L., Zhao, H., and Wong, J. (2013b) Early Paleozoic crustal anatexis in the intraplate Wuyi-Yunkai orogen, South China. Lithos 175–176, 124–145.

Wang, Q., Wyman, D.A., Xu, J.F., Dong, Y.H., Vasconcelos, P.M., Pearson, N., Wan, Y.S., Dong, H., Li, C.F., Yu, Y.S., Zhu, T.X., Feng, X.T., Zhang, Q.Y., Zi, F., and Chu, Z.Y. (2008) Eocene melting of subducting continental crust and early uplifting of central Tibet: Evidence from central-western Qiangtang high-K calc-alkaline andesites, dacites and rhyolites. Earth and Planetary Science Letters, 272, 158–171.

Wang, Y.J., Fan, W.M., Zhao, G.C., Ji, S.C., and Peng, T.P. (2007a) Zircon U-Pb geochronology of gneissic rocks in the Yunkai massif and its implications on the Caledonian event in the South China Block. Gondwana Research, 12, 404–416.

Wang, Y.J., Fan, W.M., Cawood, P.A., Ji, S.C., and Peng, T.P. (2007b) Indosinian high-strain deformation for the Yunkaidashan tectonic belt, south China: Kinematics and ^{40}Ar/^{39}Ar geochronological constraints. Tectonics, 26, TC6008.

Wang, Y.J., Zhang, A.M., Fan, W.M., Zhao, G.C., Zhang, G.W., Zhang, F.F., Zhang, Y.Z., and Li, S.Z. (2011) Kwangsian crustal anatexis within the eastern South China Block: geochemical, zircon U-Pb geochronological and Hf isotopic fingerprints from the gneissoid granites of Wugong and Wuyi-Yunkai Domains. Lithos, 127, 239–260.

Wang, Y.J., Wu, C.M., Zhang, A.M., Fan, W.M., Zhang, Y.H., Zhang, Y.Z., Peng, T.P., and Yin, C.Q. (2012) Kwangsian and Indosinian reworking of the eastern South

China Block: constraints on zircon U-Pb geochronology and metamorphism of amphibolite and granulite. Lithos, 150, 227–242.

Wang, Y.J., Fan, W.M., Zhang, G.W., and Zhang, Y.H. (2013a) Phanerozoic tectonics of the South China Block: key observations and controversies. Gondwana Research, 23, 1273–1305.

Weinberg, R.F., and Hasalová, P. (2015) Water-fluxed melting of the continental crust: A review. Lithos, 212–215, 158–188.

White, R.W., and Powell, R. (2010) Retrograde melt-residue interaction and the formation of near-anhydrous leucosomes in migmatites. Journal of Metamorphic Geology, 28, 579–597.

Wyllie, P.J., and Wolf, M.B. (1993) Amphibolite dehydration-melting: sorting out the solidus. Geological Society Special Publications, 76, 405–416.

Wolf, M.B., and Wyllie, P.J. (1994) Dehydration-melting of amphibolite at 10 kbar: the effects of temperature and time. Contributions to Mineralogy and Petrology, 115, 369–383.

Wolf, M.B., and London, D. (1995) Incongruent dissolution of REE- and Sr-rich apatite in peraluminous granitic liquids: Differential apatite, monazite, and xenotime solubilities during anataxis. American Mineralogist, 80, 765–775.

Wolfram, L.C., Weinberg, R.F., Hasalová, P., and Becchio, R. (2017) How melt segregation impacts on granite chemistry: migmatites from the Sierra de Quilmes, NW Argentina. Journal of Petrology, 58, 2239–2364.

Xu, W.G., Fan, H.R., Hu, F.F., Santoshi, M., Yang, K.F., and Lan, T.G. (2015) In situ chemical and Sr-Nd-O isotopic compositions of apatite from the Tongshi intrusive complex in the southern part of the North China Craton: Implications for petrogenesis and metallogeny. Journal of Asian Earth Sciences, 105, 208–222.

Yang, L., Liu, X.C., Wang, J.M., and Wu, F.Y. (2019) Is Himalayan leucogranite a product by in situ partial melting of the Greater Himalayan Crystalline? A comparative study of leucosome and leucogranite from Nyalam, southern Tibet. Lithos, 342–343, 542–556.

Yu, P.P., Zhang, Y.Z., Zhou, Y.Z., Weinberg, R.F., Zheng, Y., and Yang, W.B. (2019) Melt evolution of crustal anatexis recorded by the Early Paleozoic Baiyunshan migmatite-granite suite in South China. Lithos, 332–333, 83–98.

Yu, Y., Huang, X.L., He, P.L., and Li, J. (2016) I-type granitoids associated with the early Paleozoic intracontinental orogenic collapse along pre-existing block boundary in South China. Lithos, 248–251, 353–365.

Yu, Y., Huang, X.L., Sun, M., and He, P.L. (2018) Petrogenesis of granitoids and associated xenoliths in the early Paleozoic Baoxu and Enping plutons, South China: Implications for the evolution of the Wuyi-Yunkai intracontinental orogen. Journal of Asian Earth Sciences, 156, 59–74.

Zeng, L.S., Gao, L.E., Xie, K.J., and Zeng, J.L. (2011) Mid-Eocene high Sr/Y granites in the Northern Himalayan Gneiss Domes: Melting thickened lower continental crust. Earth and Planetary Science Letters, 303, 251–266.

Zeng, L.S., Saleeby, J.B., and Asimow, P. (2005) Nd isotope disequilibrium during crustal anatexis: a record from the Goat Ranch migmatite complex, southern Sierra Nevada batholith, California. Geology, 33, 53–56.

Zhang, H.F., Harris, N., Parrish, R., Kelley, S., Zhang, L., Rogers, N., Argles, T., and King, J. (2004) Causes and consequences of protracted melting of the mid-crust exposed in the North Himalayan antiform. Earth and Planetary Science Letters, 228, 195–212.

Zhao, K., Xu, X.S., Erdmann, S., Liu, L., and Xia, Y. (2017a). Rapid migration of a magma source from mid- to deep-crustal levels: Insights from restitic granulite enclaves and anatectic granite. Geological Society of America Bulletin, 129(11–12), 1708–1725.

Zhao, K., Xu, X.S., and Erdmann, S. (2017b). Crystallization conditions of peraluminous charnockites: constraints from mineral thermometry and thermodynamic modelling. Contributions to Mineralogy and Petrology, 172, 26.

Zheng, Y.C., Hou, Z.Q., Fu, Q., Zhu, D.C., Liang, W., and Xu, P.Y. (2016) Mantle inputs to Himalayan anatexis: Insights from petrogenesis of the Miocene Langkazi leucogranite and its dioritic enclaves. Lithos, 264, 125–140.

FIGURE CAPTIONS

Fig. 1 (a) Simplified regional map showing the tectonic framework of the South China Block that comprises the Yangtze Block in the northwest and the Cathaysia

Block in the southeast; (b) Simplified geological map of the Yunkai domain (revised from Lin et al., 2008; Wang et al., 2013a; Yu et al., 2018) showing the sample location (Jindong).

Fig. 2 Photographs showing (a) granitic melt segregation from the melanosome forming felsic dykes with inserted chart showing distribution of leucosomes, including lenticular (L) and net-strutured types (N); (b) gneissic foliation of the Jindong migmatite containing biotite-poor lenticular leucosomes parallel to foliation, which are embedded in the biotite-rich melanosome; (c) lenticular leucosome bordered by biotite-rich melanosome; (d) thin lenticular leucosome feeding into felsic veins, forming net-structured leucosomes, which are discordant with the foliation; (e) aggregation of lenticular leucosome into the net-structured leucosome and the edge showing transitional contact with melanosome; and (f) the net-structured leucosomes showing transitional contact with melanosome at the edge.

Fig. 3 Sample photograph and microphotographs: (a, b) leucosome lens containing biotite relicts captured from the surrounding biotite-rich residuum; (c) corroded margin of K-feldspar, plagioclase and biotite with margin of K-feldspar replaced by albite in melanosome; (d) corroded margin of biotite and muscovite in the melanosome; (e) entrained biotite with corroded margin in the lenticular leucosome; (f) occurrence of muscovite along the margin of K-feldspar and plagioclase in lenticular leucosome; and (g) net-structured leucosome containing rectangular plagioclase and anhedral quartz, K-feldspar, muscovite and altered biotite. Mineral abbreviation: Bt = biotite; Ms = muscovite; Pl = plagioclase; Ab = albite; Kfs = K-feldspar; Qz = quartz.

Fig. 4 X-ray element distribution map and BSE image showing the melting-related texture in the Jindong melanosome: (a) Corroded margin of plagioclase replaced by quartz; (b)-(d) Reactant K-feldspar, biotite and muscovite showing erosion on the margin, which were replaced by albite that contains K-feldspar and biotite relicts; (e) Dissolution of apatite with monazite precipitation during melting in melanosome; and (f) Fine-grained xenotime crystallizing around apatite. Mineral abbreviation: Bt = biotite; Ms = muscovite; Ilm = ilmenite; Pl = plagioclase; Kfs = K-feldspar; Qz = quartz; Ap = apatite; Mnz = monazite; Xtm = xenotime.

Fig. 5 Cathodoluminescence (CL) images and U-Pb concordia diagrams of zircons from the Jindong melanosome (YK17-56) and net-structured (N) leucosome (YK17-59). CL images show inner structure of representative zircons with analytical spot (red circles).

Fig. 6 Bivariate element plots of TiO_2 + Fe_2O_3 + MgO versus (a) K_2O; (b) Na_2O; (c) Ba and (d) Sr for the Jindong melanosome, lenticular (L) and net-structured (N) leucosomes. The orange star symbol represents average composition of lenticular leucosome. Bt = biotite; Ms = muscovite; Pl = plagioclase; Qz = quartz.

Fig. 7 Chondrite-normalized REE patterns and primitive mantle -normalized multi-element variation diagrams for the Jindong melanosome, lenticular (L) and net-structured (N) leucosomes. Chondrite and primitive mantle values are from Sun and McDonough (1989) and McDonough and Sun (1995), respectively.

Fig. 8 Diagrams of (a) Nb vs. Rb of biotite; (b) Ba vs. Rb of muscovite; (c) Ba vs. Sr of plagioclase; and (d) Ba vs. Rb of K-feldspar in the Jindong melanosome, leuticular (L) leucosome and net-structured (N) leucosome.

Fig. 9 Diagrams of (a) Ba vs. Rb; (b) Sr vs. Rb and (c) Rb/Sr vs. Ba for the Jindong melanosome, lenticular (L) and net-structured (N) leucosomes. Biotite (Bt), Muscovite (Ms), plagioclase (Pl), K-feldspar (Kfs) and quartz (Qz) are average composition of respective minerals from the melanosome (Table A6). The trends of fractional crystallization of Kfs + Pl in different proportions (25%, 50%, 75% Kfs) are calculated based on partition coefficients from Ewart and Griffin (1994). Data of the Himalayan leucogranites are compiled from Guo et al. (2012), King et al. (2011), Liu et al. (2014, 2016), Singh et al. (2016), Visonà et al. (2002), Yang et al. (2019), Zeng et al. (2011), Zhang et al. (2004), Zheng et al. (2016). Data of the Triassic granites are from Gao et al, (2017). The Middle Paleozoic granites in the Tasman Orogen mainly include those in Victoria, Australia (Hergt et al., 2007; Clemens et al., 2017, 2018; Iles et al., 2020).

Fig. 10 Contributions of (a) major phases, (b) zircon and (c) apatite in the Jindong melanosome to the leucosome trace element compositions during anatexis. Major phases include biotite (Bt), muscovite (Ms), K-feldspar (Kfs), plagioclase (Pl), and quartz (Qz). The proportion of trace element of major phases are calculated based on melting reaction of "0.033Bt + 0.01Ms+0.347Qz + 0.41Kfs + 0.20Pl = 1 melt" and average compositions of major minerals in melanosome (Tables A5, A6). Contributions of apatite and zircon are calculated based on their average composition in melanosome sample YK17-56 (Table A6) assuming that P_2O_5 and Zr in the melt are dominated by dissolution of apatite and zircon, respectively. Detailed calculation is compiled in Table A8.

Fig. 11 Diagrams of (a) La vs. P_2O_5; (b) Yb vs. P_2O_5; (c) Th vs. P_2O_5; and (d) Y vs. P_2O_5 for the Jindong melanosome, lenticular (L) and net-structured (N) leucosomes. The dotted lines represent dissolution of monazite (Mnz) + xenotime (Xtm) + apatite (Ap), with assemblage of 71.8%Ap + 15%Xtm ($[Y_{0.963}Yb_{0.037}]\ PO_4$) + 13.2% Mnz ($[La_{1.33}Nd_{1.14}Th_{0.53}]\ [PO_4]_3$). The trends marking the precipitation of monazite and xenotime with increasing P_2O_5 content in melts are represented by the dark blue lines and calculated based on Eq. 3, with 0.0135%Mnz + 0.0165%Xtm precipitating as 1%Ap dissolution, respectively. The trends of apatite dissolution are calculated based on average composition of apatite in sample YK17-56 (Table A6). Data sources for Himalayan (HM) leucogranite are the same as in Fig. 9, which are shown by the light blue shaded area. Compositions of primitive melts (PM) are calculated by the melting reaction Eq. 2. Data for Tibet adakite are from Wang et al. (2008).

Fig. 12 (a) $\varepsilon_{Nd}(t)$ vs. age for the Jindong melanosome, lenticular (L), net-structured (N) leucosomes and apatite (Ap) in melanosome. $\varepsilon_{Nd}(t)$ of apatite and whole-rock for the Jindong melanosome were calculated for 437 Ma and 238 Ma, respectively, to show their Nd isotopic compositions during emplacement of the protolith during the Early Paleozoic and anatexis during Triassic, separately. (b) Whole-rock $\varepsilon_{Nd}(t)$ vs. P_2O_5; (c) Whole-rock $\varepsilon_{Nd}(t)$ vs. Nd content. The primitive melts (PM) represent melts formed through breakdown of major minerals, which were calculated based on the melting reaction Eq. 2 and average composition of major phases with $\varepsilon_{Nd}(t)$ value of -9.6. Mineral compositions of monazite (Mnz) and apatite (Ap) are the same as in Fig. 11. $\varepsilon_{Nd}(t)$ of apatite is represented by *in situ* apatite $\varepsilon_{Nd}(t)$ values (-13.2) of YK17-56-11 (Table A7). $\varepsilon_{Nd}(t)$ of monazite is assumed to be -9.6, because monazite is the major host of Nd in melanosome. Numbers along the trend lines represent the proportion of monazite in dissolved phosphate minerals (monazite + apatite). Data sources of the Himalayan (HM) leucogranites and Triassic granites of the Guangxi province in the South China Block are the same as in Fig. 9.

Fig. 13 Cartoons showing (a) generation of melt (M) along boundary and corner of minerals (Eq. 1) and interaction between melt and apatite releasing P into melt and extracting Th, Y and REE because of precipitation of monazite and xenotime (Eq. 3); and (b) Fractional crystallization of Kfs and Pl during the melt segregation resulting in fractionation between Rb, Sr and Ba. Mineral abbreviations: Bt = biotite; Ms = muscovite; Pl = plagioclase; Kfs = K-feldspar; Qz = quartz; Ap = apatite; Mnz = monazite; Xtm = xenotime.

Fig. 1

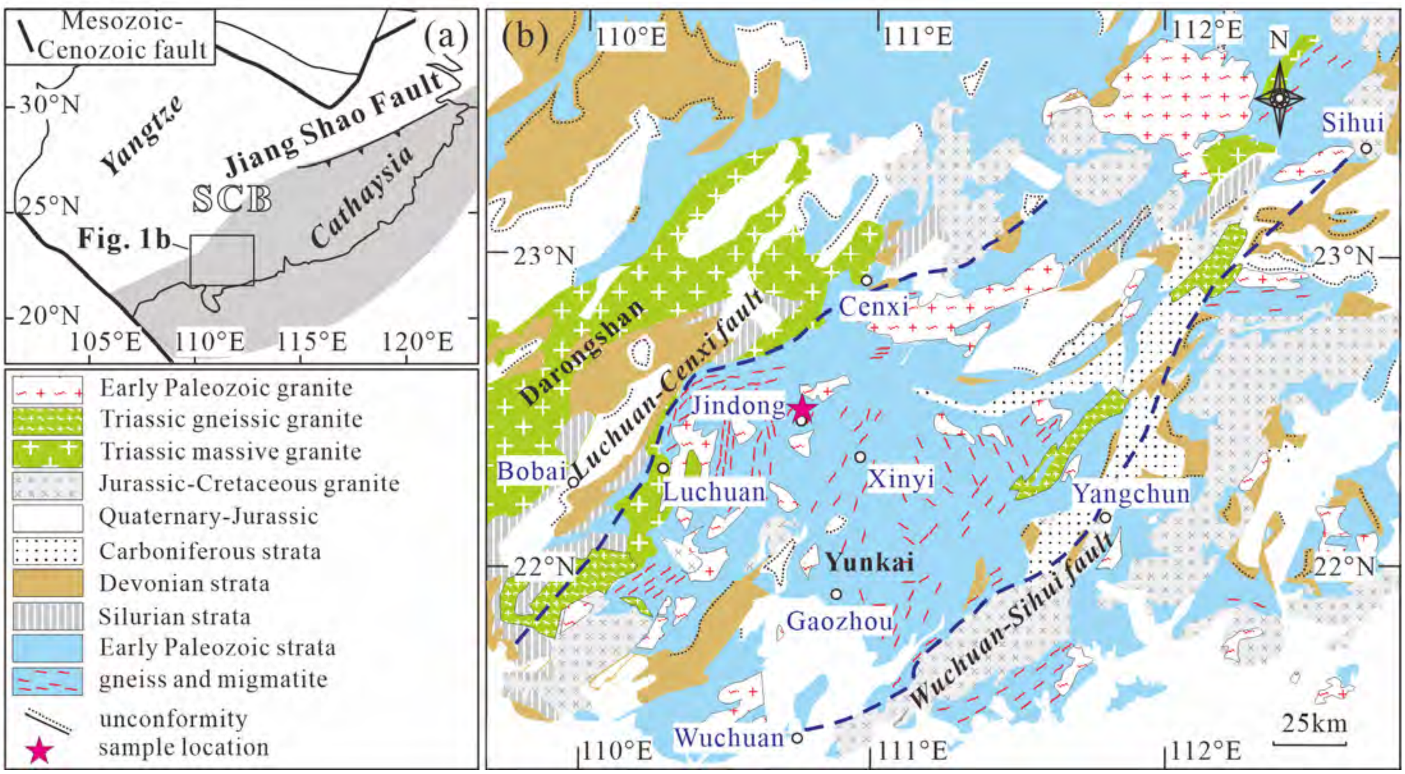
Mesozoic-Cenozoic fault
(a)
30°N
25°N
20°N
105°E
110°E
115°E
120°E
Yangtze
Jiang Shao Fault
SCB
Cathaysia
Fig. 1b
Early Paleozoic granite
Triassic gneissic granite
Triassic massive granite
Jurassic-Cretaceous granite
Quaternary-Jurassic
Carboniferous strata
Devonian strata
Silurian strata
Early Paleozoic strata
gneiss and migmatite
unconformity
sample location
(b)
110°E
111°E
112°E
N
23°N
22°N
Sihui
Darongshan
Luchuan-Cenxi fault
Cenxi
Jindong
Bobai
Luchuan
Xinyi
Yangchun
Yunkai
Gaozhou
Wuchuan-Sihui fault
Wuchuan
25km

Fig. 2

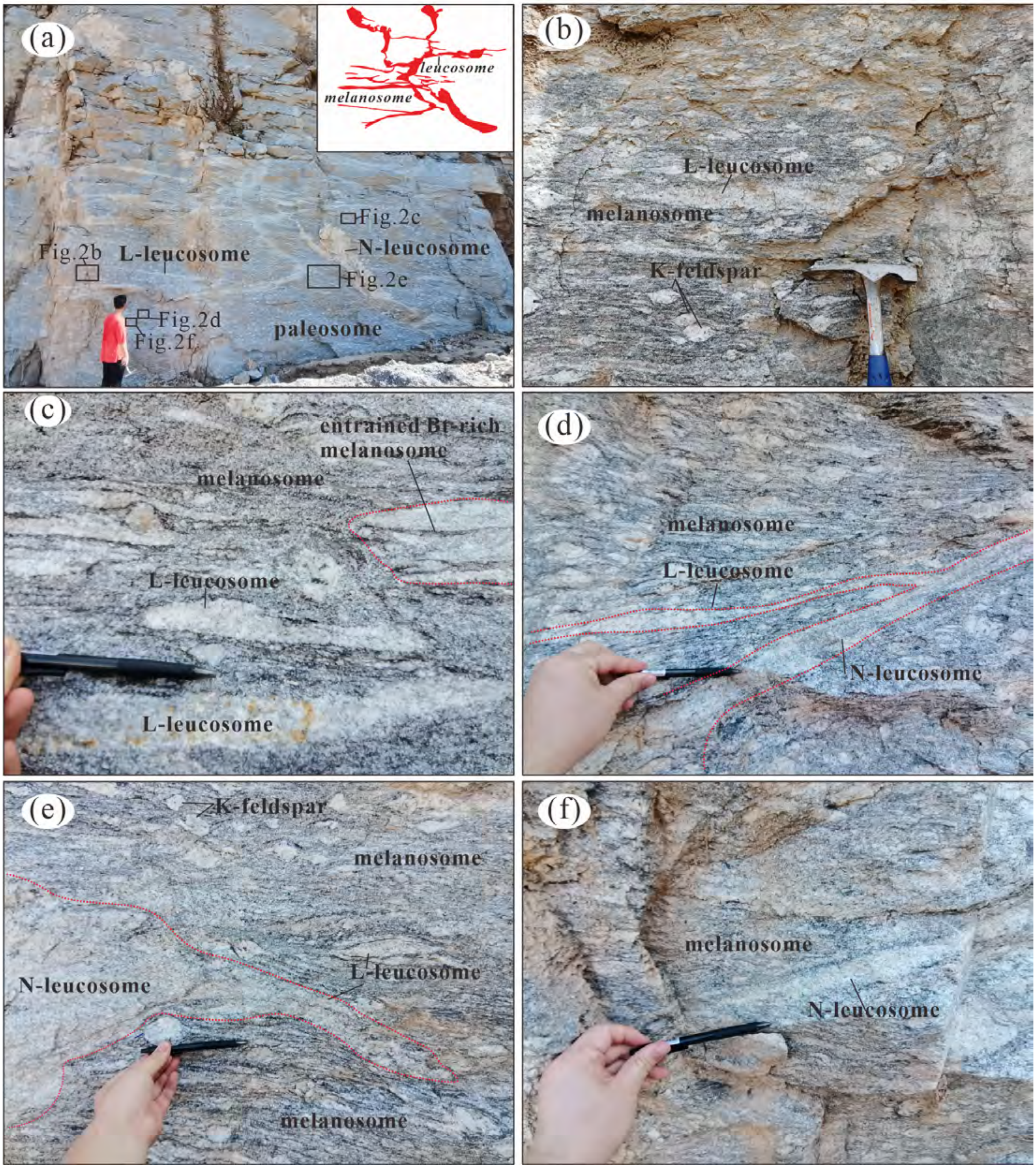
(a)
leucosome
melanosome
Fig.2b
L-leucosome
Fig.2c
N-leucosome
Fig.2e
Fig.2d
Fig.2f
paleosome
(b)
L-leucosome
melanosome
K-feldspar
(c)
entrained Bt-rich melanosome
melanosome
L-leucosome
L-leucosome
(d)
melanosome
L-leucosome
N-leucosome
(e)
K-feldspar
melanosome
N-leucosome
L-leucosome
melanosome
(f)
melanosome
N-leucosome

DOI: https://doi.org/10.2138/am-2022-8594. http://www.minsocam.org/

Fig. 3

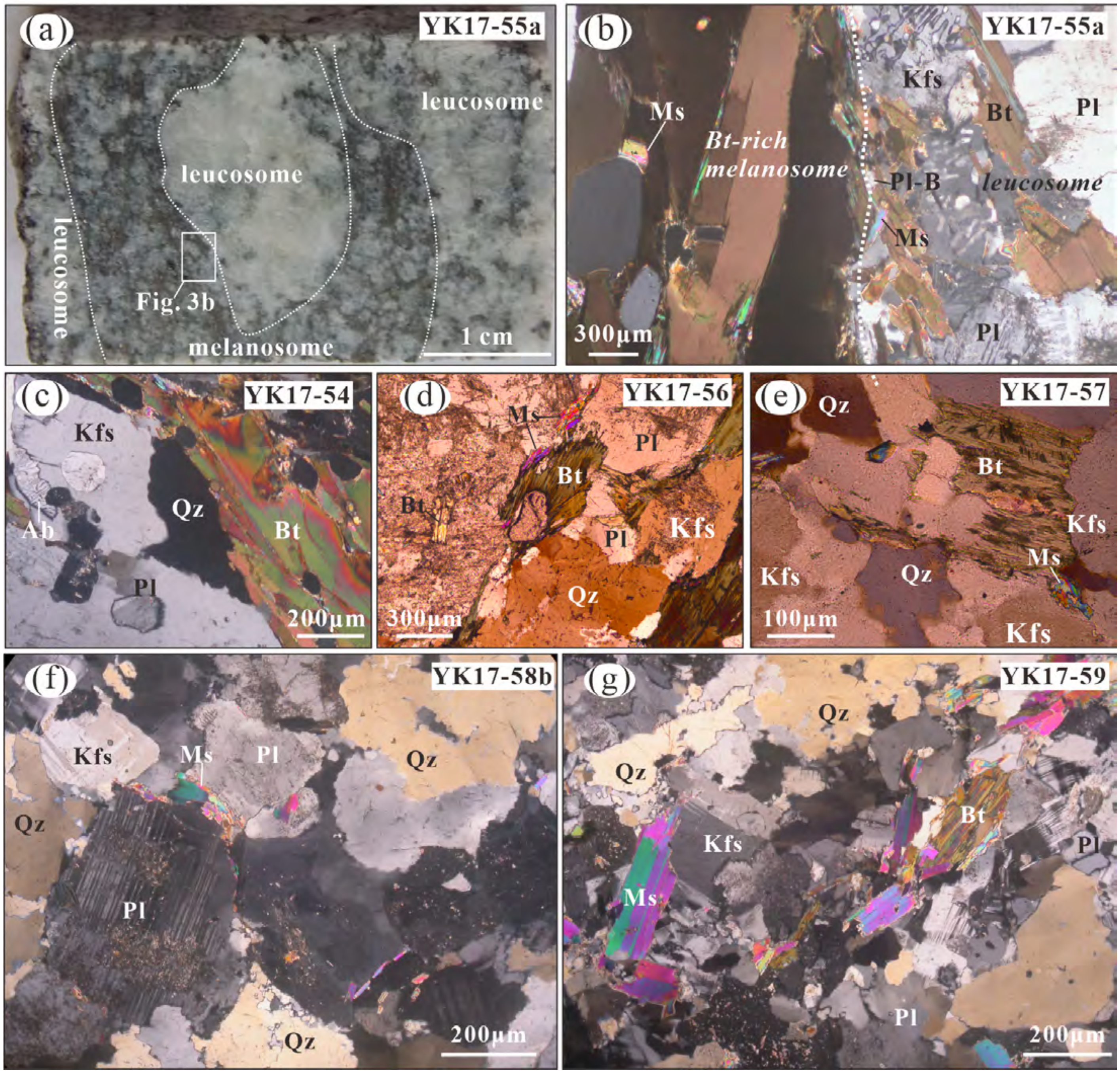

This is the peer-reviewed, final accepted version for American Mineralogist, published by the Mineralogical Society of America.
The published version is subject to change. Cite as Authors (Year) Title. American Mineralogist, in press.
DOI: https://doi.org/10.2138/am-2022-8594. http://www.minsocam.org/

Fig. 4

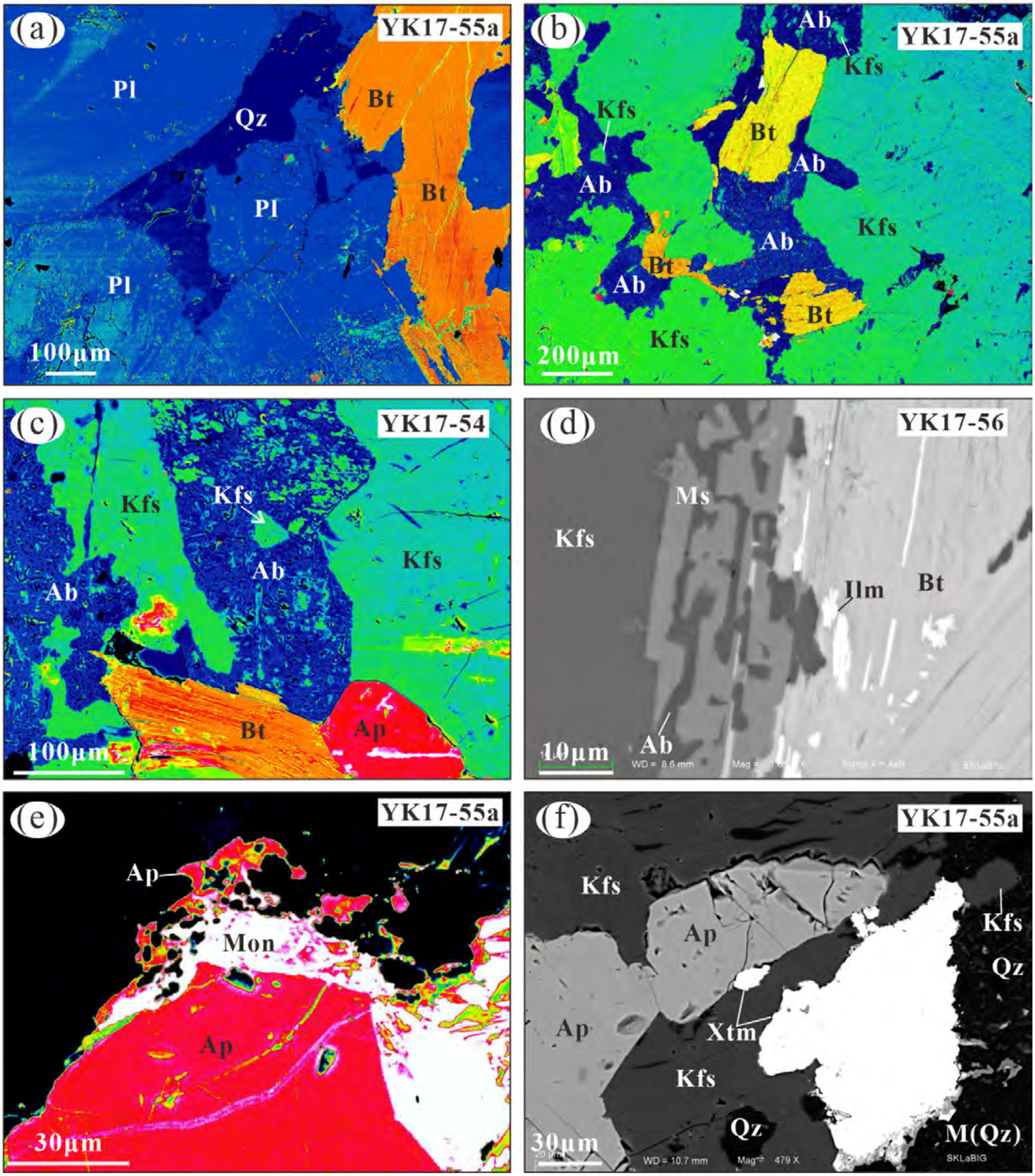

This is the peer-reviewed, final accepted version for American Mineralogist, published by the Mineralogical Society of America.
The published version is subject to change. Cite as Authors (Year) Title. American Mineralogist, in press.
DOI: https://doi.org/10.2138/am-2022-8594. http://www.minsocam.org/

Fig. 5

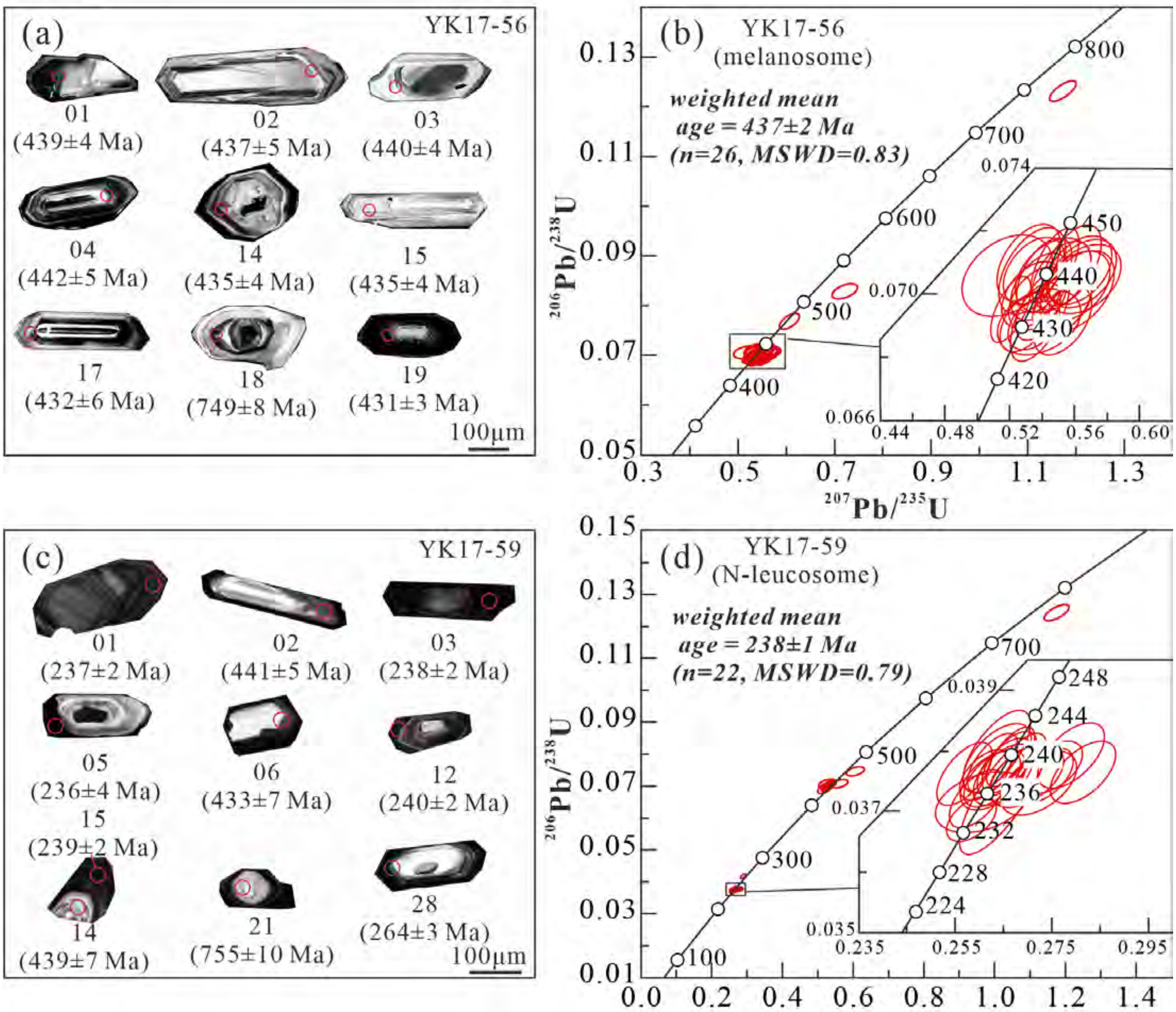

This is the peer-reviewed, final accepted version for American Mineralogist, published by the Mineralogical Society of America.
The published version is subject to change. Cite as Authors (Year) Title. American Mineralogist, in press.
DOI: https://doi.org/10.2138/am-2022-8594. http://www.minsocam.org/

Fig. 6

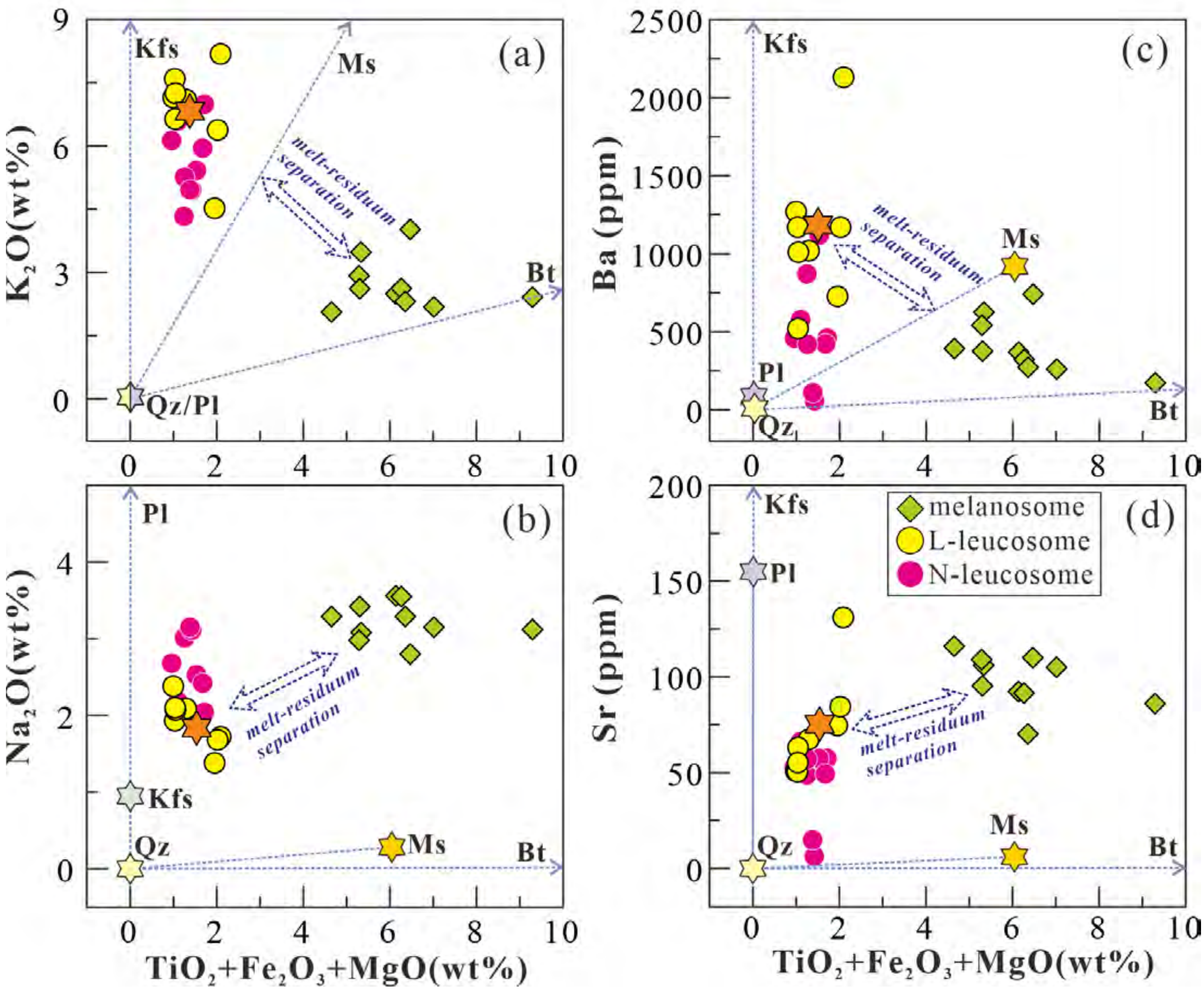

DOI: https://doi.org/10.2138/am-2022-8594. http://www.minsocam.org/

Fig. 7

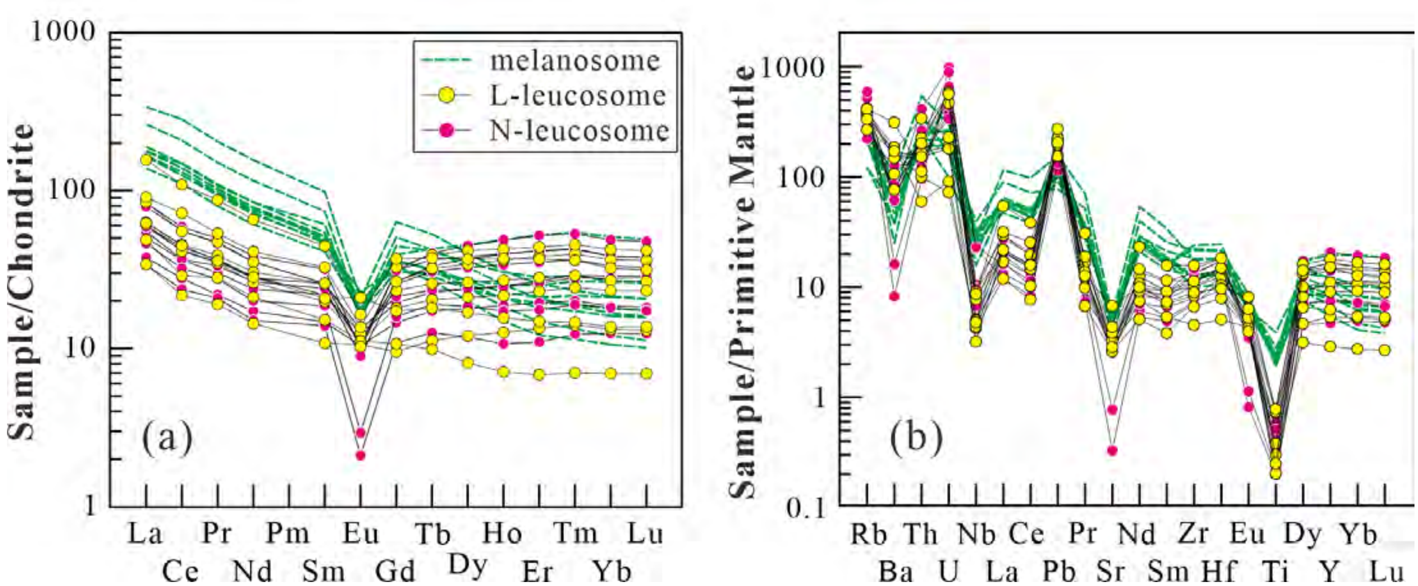

Fig. 8

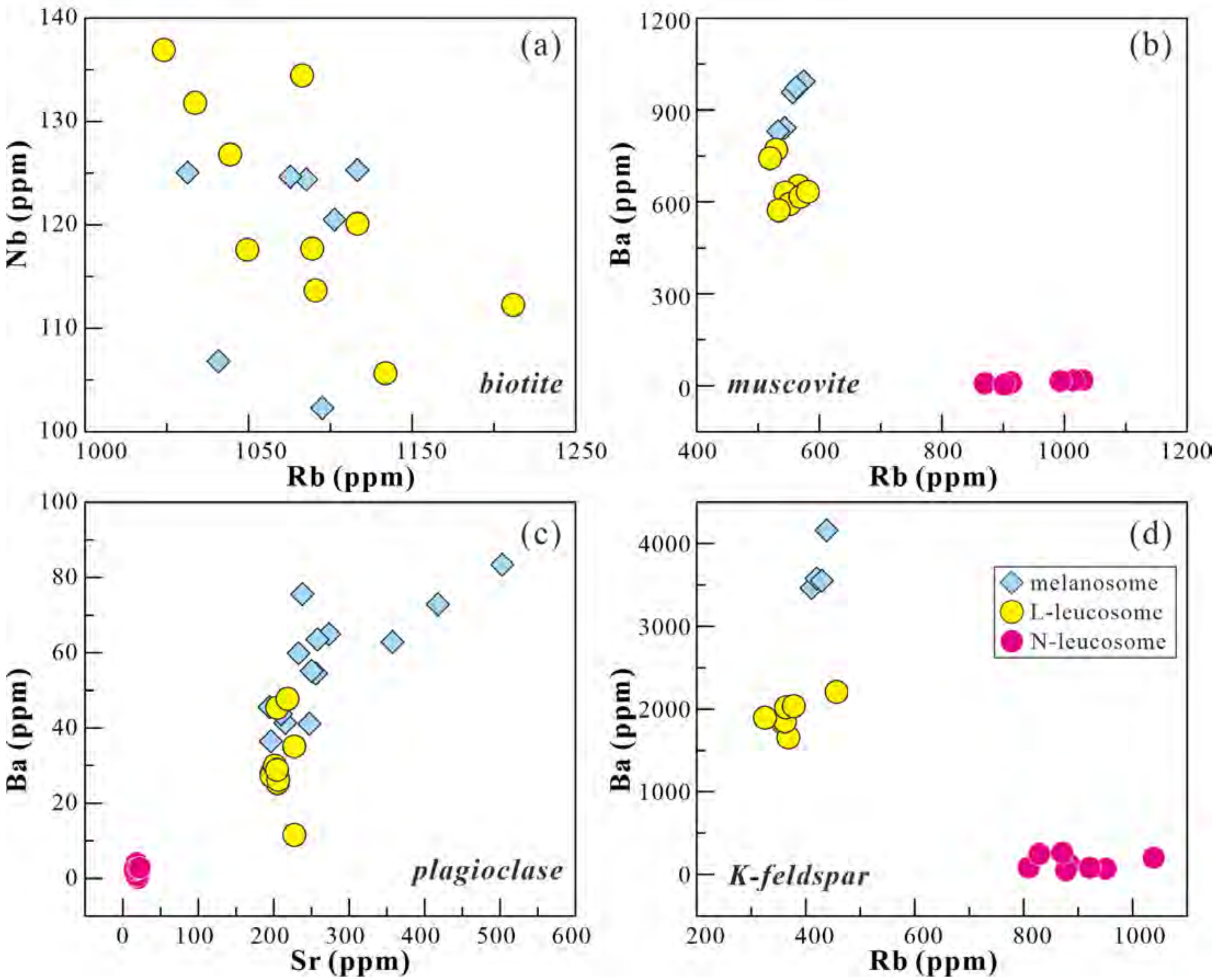
(a)
biotite
Nb (ppm)
Rb (ppm)
140
130
120
110
100
1000
1050
1150
1250
(b)
muscovite
Ba (ppm)
Rb (ppm)
1200
900
600
300
0
400
600
800
1000
1200
(c)
plagioclase
Ba (ppm)
Sr (ppm)
100
80
60
40
20
0
0
100
200
300
400
500
600
(d)
K-feldspar
Ba (ppm)
Rb (ppm)
4000
3000
2000
1000
0
200
400
600
800
1000
melanosome
L-leucosome
N-leucosome

DOI: https://doi.org/10.2138/am-2022-8594. http://www.minsocam.org/

Fig. 9

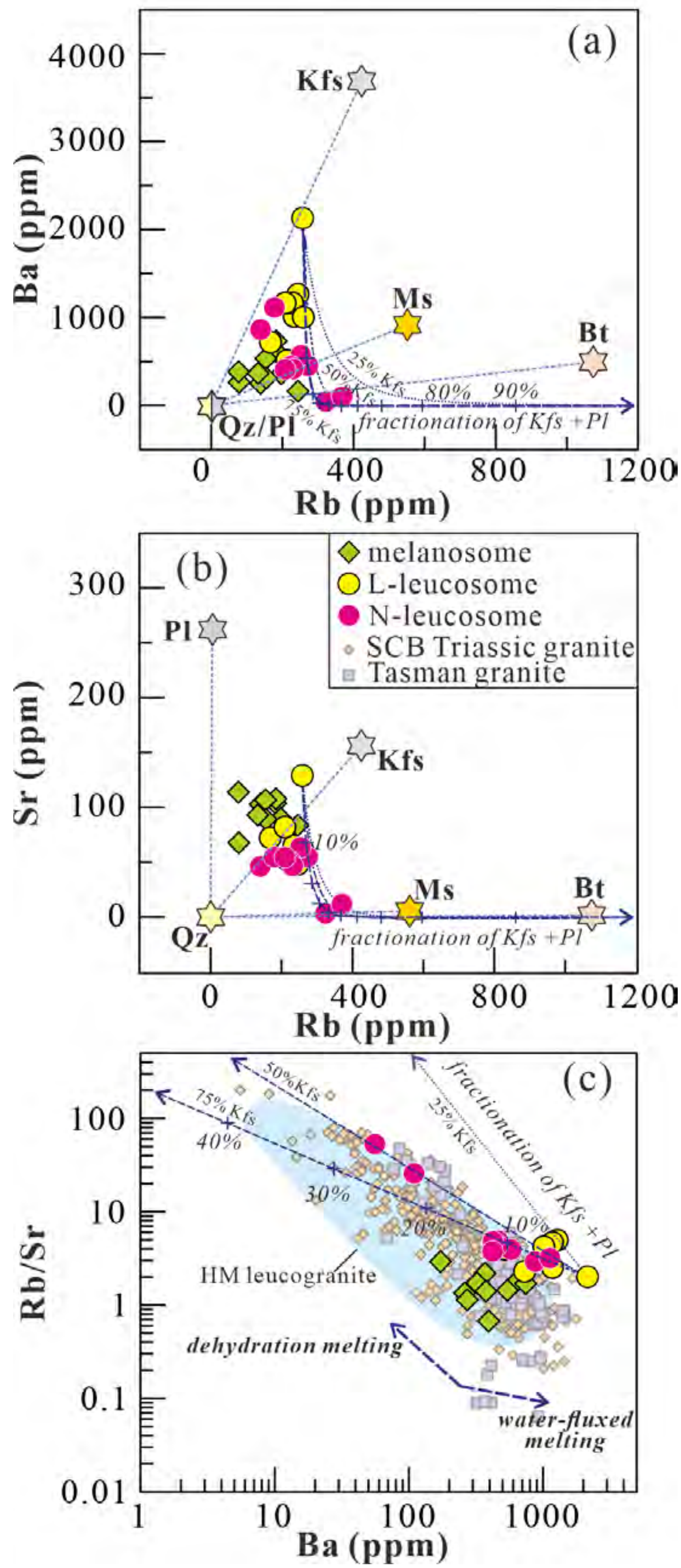

Fig .10

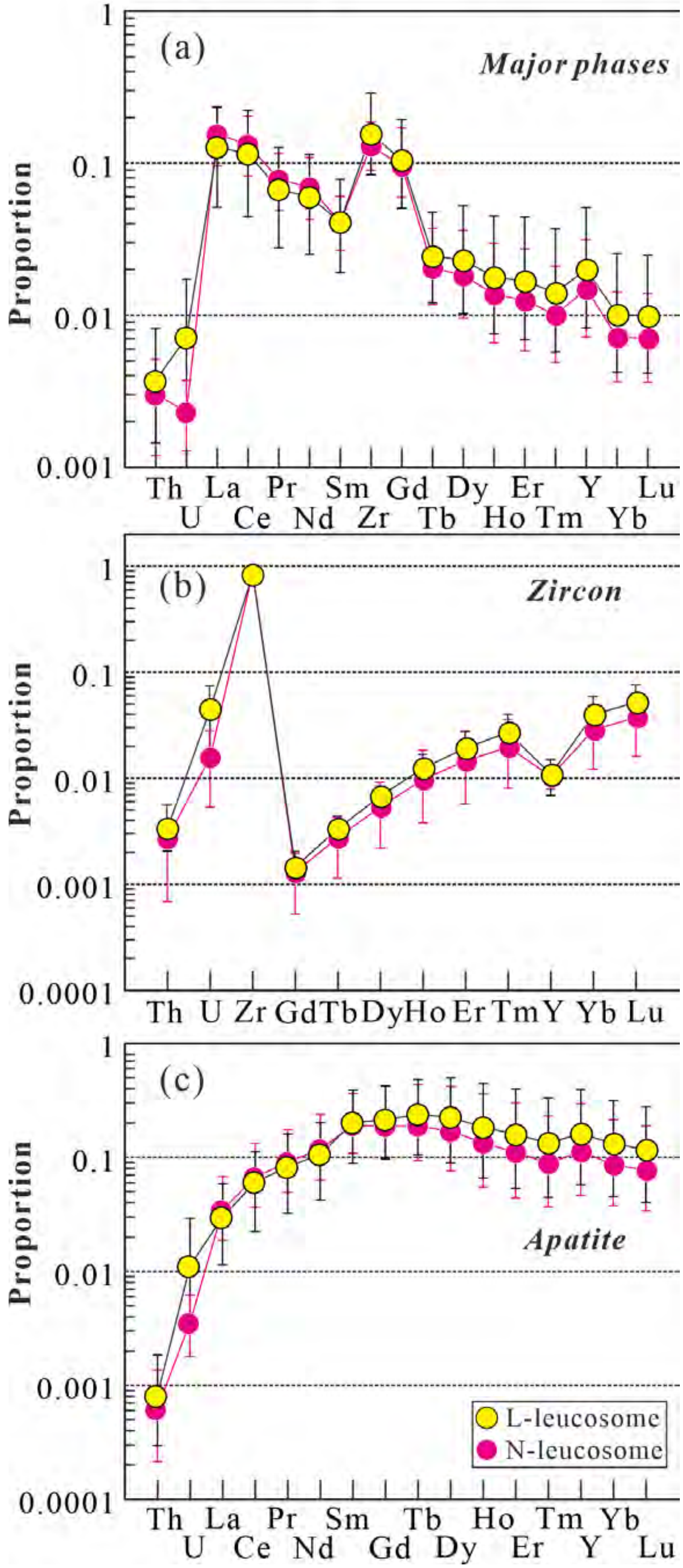
(a)
Major phases
Proportion
1
0.1
0.01
0.001
Th U La Ce Pr Nd Sm Zr Gd Tb Dy Ho Er Tm Y Yb Lu
(b)
Zircon
Proportion
1
0.1
0.01
0.001
0.0001
Th U Zr Gd Tb Dy Ho Er Tm Y Yb Lu
(c)
Apatite
Proportion
1
0.1
0.01
0.001
0.0001
L-leucosome
N-leucosome
Th U La Ce Pr Nd Sm Gd Tb Dy Ho Er Tm Y Yb Lu

DOI: https://doi.org/10.2138/am-2022-8594. http://www.minsocam.org/

Fig .11

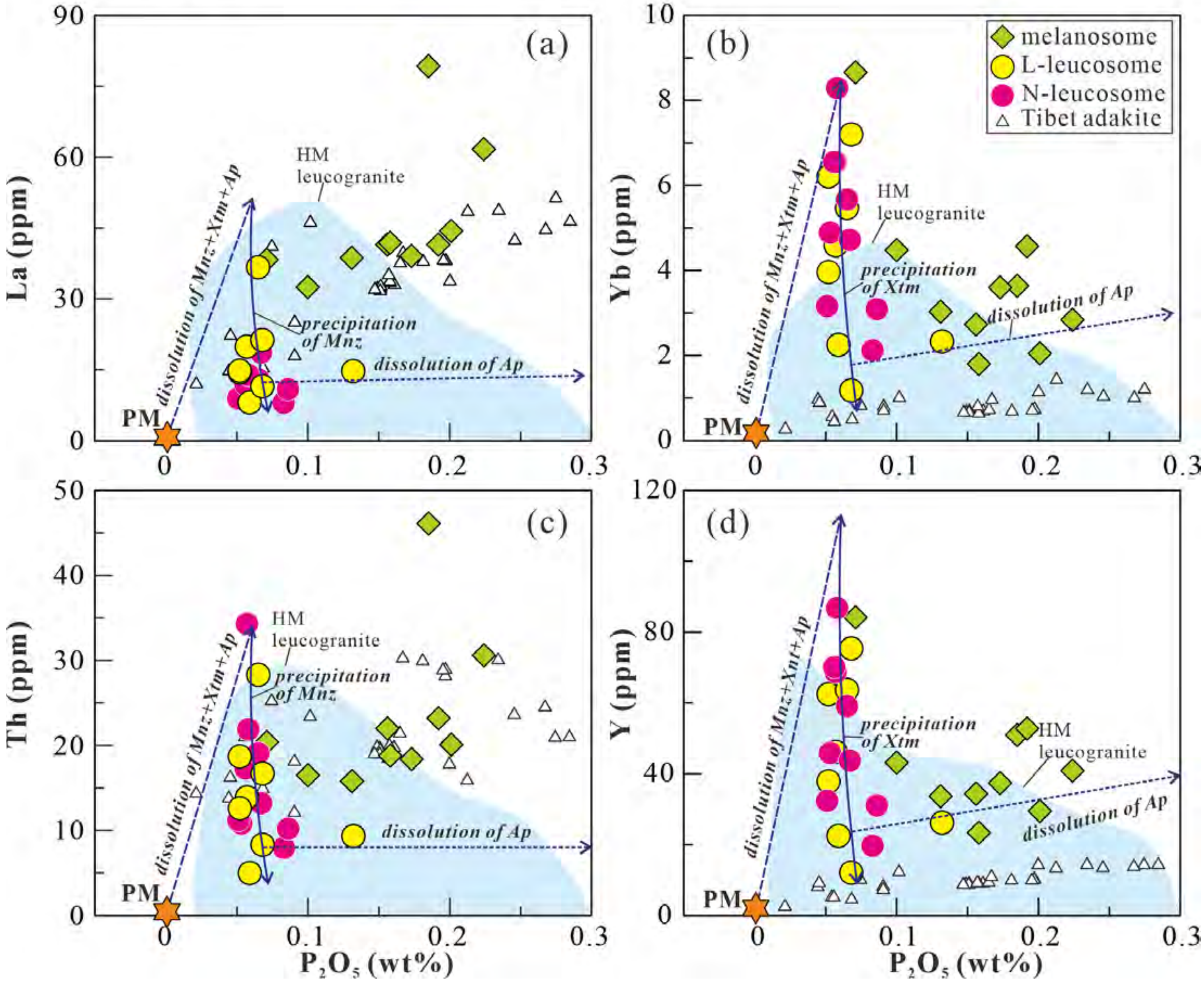

DOI: https://doi.org/10.2138/am-2022-8594. http://www.minsocam.org/

Fig .12

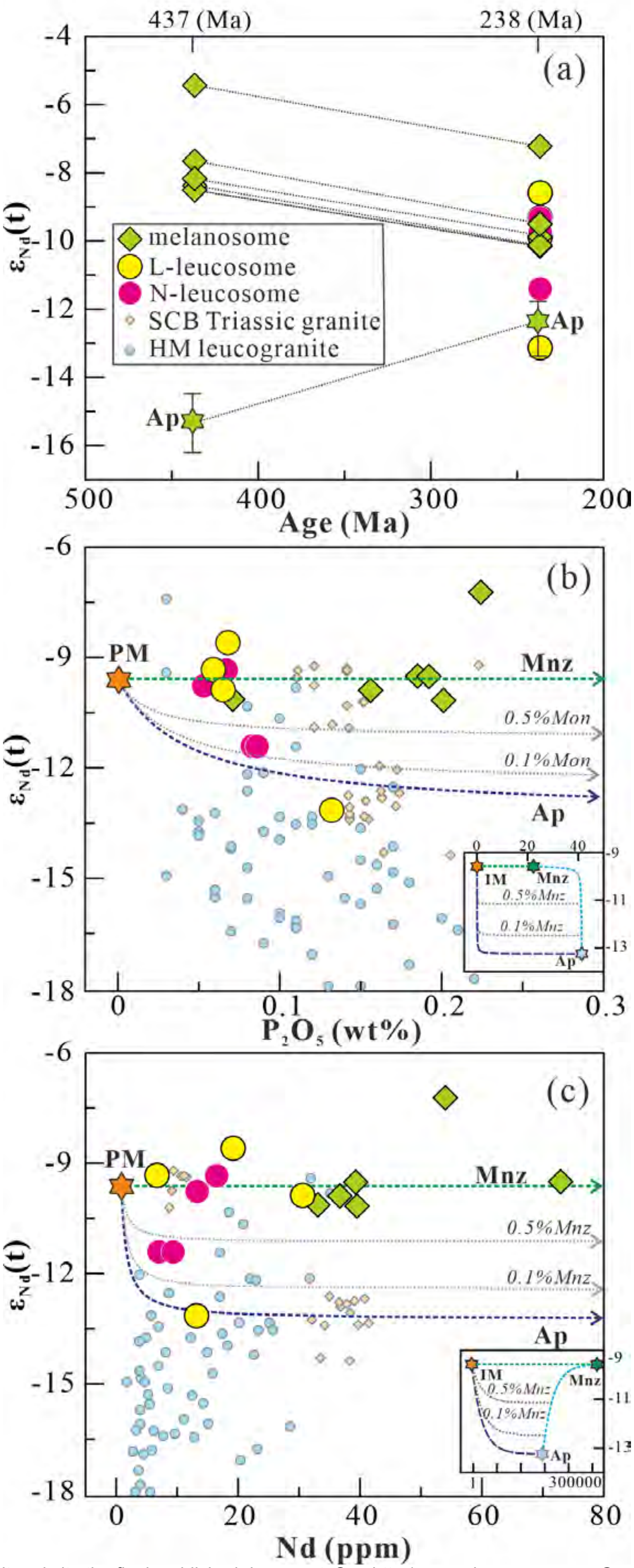

Fig .13

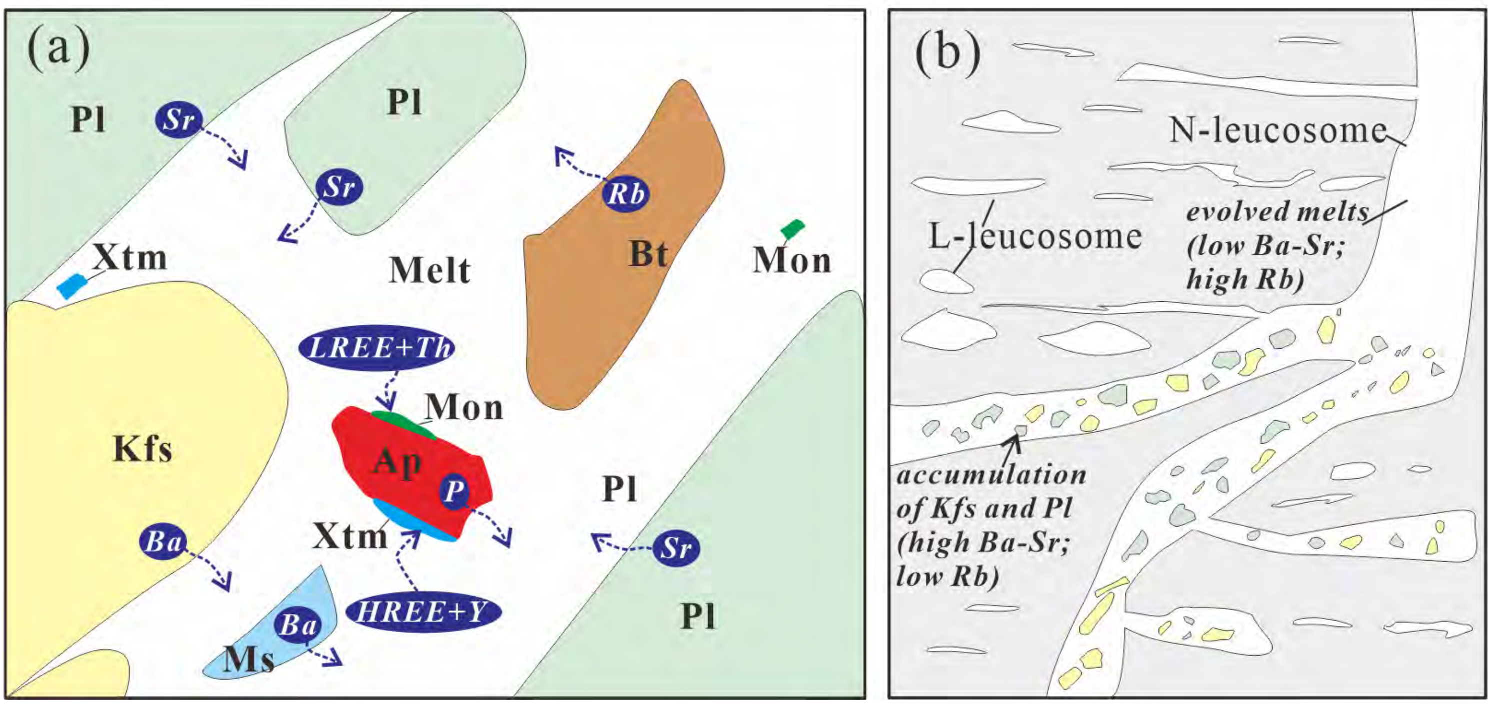
(a)
Pl
Sr
Pl
Sr
Rb
Xtm
Melt
Bt
Mon
LREE+Th
Mon
Kfs
Ap
P
Pl
Xtm
Ba
Sr
Ba
HREE+Y
Pl
Ms
(b)
N-leucosome
evolved melts
(low Ba-Sr;
high Rb)
L-leucosome
accumulation
of Kfs and Pl
(high Ba-Sr;
low Rb)